Flow and transport in fractured poroelastic media

Ilona Ambartsumyan, Eldar Khattatov, Truong Nguyen & Ivan Yotov

GEM - International Journal on Geomathematics

ISSN 1869-2672
Volume 10
Number 1

Int J Geomath (2019) 10:1-34
DOI 10.1007/s13137-019-0119-5

Springer

GEM - International Journal on Geomathematics (2019) 10:11
https://doi.org/10.1007/s13137-019-0119-5

ORIGINAL PAPER

Flow and transport in fractured poroelastic media

Ilona Ambartsumyan[1] · **Eldar Khattatov**[1] · **Truong Nguyen**[1] · **Ivan Yotov**[1]

Received: 13 April 2018 / Accepted: 4 December 2018

Abstract
We study flow and transport in fractured poroelastic media using Stokes flow in the fractures and the Biot model in the porous media. The Stokes–Biot model is coupled with an advection–diffusion equation for modeling transport of chemical species within the fluid. The continuity of flux on the fracture-matrix interfaces is imposed via a Lagrange multiplier. The coupled system is discretized by a finite element method using Stokes elements, mixed Darcy elements, conforming displacement elements, and discontinuous Galerkin for transport. The stability and convergence of the coupled scheme are analyzed. Computational results verifying the theory as well as simulations of flow and transport in fractured poroelastic media are presented.

Keywords Fluid-poroelastic structure interaction · Stokes-Biot model · Coupled flow and transport · Fractured poroelastic media

Mathematics Subject Classification 76S05 · 76D07 · 74F10 · 65M60 · 65M12

1 Introduction

Flow and transport in fractured poroelastic media occur in many applications, including enhanced oil and gas recovery, hydraulic fracturing, groundwater hydrology, and

Partially supported by DOE Grant DE-FG02-04ER25618 and NSF Grants DMS 1418947 and DMS 1818775.

✉ Ivan Yotov
yotov@math.pitt.edu

Ilona Ambartsumyan
ila6@pitt.edu

Eldar Khattatov
elk58@pitt.edu

Truong Nguyen
tqn4@pitt.edu

[1] Department of Mathematics, University of Pittsburgh, Pittsburgh, PA 15260, USA

Published online: 29 January 2019

subsurface waste repositories. These are challenging multiphysics processes involving interaction between a free fluid in the fractures with a fluid within the porous medium. The fluid flow may cause and be affected by solid deformation. For example, geomechanics effects are critical in hydraulic fracturing, as well as in modeling phenomena such as subsidence and compaction. Furthermore, the flow process may be coupled with transport phenomena, with the substance of interest propagating both through the fracture network and the porous matrix. Typical examples include tracking and cleaning up groundwater contaminants, leakage of subsurface radioactive waste, and proppant injection in hydraulic fracturing.

We use the Stokes equations to model the free fluid in the fractures and the Biot poroelasticity model (Biot 1941) for the fluid in the poroelastic region. The latter is based on a linear stress-strain constitutive relationship for the porous solid, and Darcy's law, which describes the average velocity of the fluid in the pores. The interaction across the fracture-matrix interfaces exhibits features of both Stokes–Darcy coupling (Discacciati et al. 2002; Girault and Rivière 2009; Layton et al. 2003; Rivière and Yotov 2005; Vassilev et al. 2014) and fluid–structure interaction (FSI) (Galdi and Rannacher 2010; Bazilevs et al. 2013; Bungartz and Schäfer 2006; Formaggia et al. 2010; Richter 2017). We refer to the Stokes–Biot coupling considered in this paper as fluid–poroelastic structure interaction (FPSI). There has been growing interest in such models in the literature. The well-posedness of the mathematical model was studied in Showalter (2005). Numerical studies include variational multiscale methods for the monolithic system and iterative partitioned scheme (Badia et al. 2009), a non-iterative operator-splitting method (Bukac et al. 2015), a partitioned method based on Nitsche's coupling (Bukac et al. 2015), and a Lagrange multiplier formulation for the continuity of flux (Ambartsumyan et al. 2018b).

To simplify the presentation we consider a fixed domain in time. As presented, the model is suitable for deformations that are small relative to the width of the fractures. This is valid for scales that are zoomed-in on the fractures or for meso-scale inclusions such as cavities. The model can be extended to account for the motion of the fluid domain by using the Arbitrary Lagrangian-Eulerian (ALE) approach, which has been done in Badia et al. (2009) and Bukac et al. (2015).

In this work we employ a monolithic scheme for the full-dimensional Stokes–Biot problem to model flow in fractured poroelastic media. We note that an alternative approach is based on a reduced-dimension fracture model, including the Reynolds lubrication equation (Ganis et al. 2014; Girault et al. 2015; Lee et al. 2016b; Mikelić et al. 2015) and an averaged Brinkman equation (Bukac et al. 2017). Works that do not account for elastic deformation of the media include averaged Darcy models (Martin et al. 2005; Frih et al. 2012; Morales and Showalter 2010; D'Angelo and Scotti 2012; Fumagalli and Scotti 2012; Boon et al. 2018; Flemisch et al. 2018), Forchheimer models (Frih et al. 2008), Brinkman models (Lesinigo et al. 2011), and an averaged Stokes model that results in a Brinkman model for the fracture flow (Morales and Showalter 2017).

For the discretization of the full-dimensional Stokes–Biot problem we consider the mixed formulation for Darcy flow in the Biot system, which provides a locally mass conservative flow approximation and an accurate Darcy velocity. This formulation results in the continuity of normal velocity condition being of essential type,

which is enforced through a Lagrange multiplier (Ambartsumyan et al. 2018b). The discretization allows for the use of any stable Stokes spaces in the fracture region and any stable mixed Darcy spaces (Boffi et al. 2013). For the elasticity equation we employ a displacement formulation with continuous Lagrange elements.

The Stokes–Biot system is coupled with an advection diffusion equation for modeling transport of chemical species within the fluid. The transport equation is discretized by a discontinuous Galerkin (DG) method. DG methods (Arnold et al. 2001; Oden et al. 1998; Rivière et al. 1999; Cockburn and Shu 1998; Sun and Wheeler 2005b) exhibit local mass conservation, reduced numerical diffusion, variable degrees of approximation, and accurate approximations for problems with discontinuous coefficients. Due to their low numerical diffusion, DG methods are especially suited for advection–diffusion problems (Cockburn and Shu 1998; Cockburn and Dawson 2002; Sun and Wheeler 2005b; Dawson et al. 2004; Wheeler and Darlow 1980; Aizinger et al. 2000). Coupled Darcy flow and transport problems utilizing DG for transport have been studied in Sun and Wheeler (2005a), Sun et al. (2002), Dawson (1999) and Wheeler and Darlow (1980). Coupling of Stokes–Darcy flow with transport using a local discontinuous Galerkin scheme was developed in Vassilev and Yotov (2009). A coupled phase field-transport model for proppant-filled fractures is studied in Lee et al. (2016a). A flow-transport reduced fracture model using Darcy flow in the fracture and the matrix is developed in Fumagalli and Scotti (2013). To the best of our knowledge, the coupled Stokes–Biot-transport problem has not been studied in the literature. Here we follow the approach from Sun et al. (2002) for miscible displacement in porous media and employ the non-symmetric interior penalty Galerkin (NIPG) method for the transport problem. We note that the dispersion tensor in the transport equation is a nonlinear function of the velocity. The work in Sun et al. (2002) handles this difficulty by utilizing a cut-off operator. Here we avoid the need for the cut-off operator by establishing an L^∞-bound for the computed Stokes–Biot velocity. As a result, the velocity is directly incorporated into the transport scheme. We present a stability bound and an error estimate for the solution of the transport equation. The analysis in this paper is presented for saturated flow and linear transport. Extensions to unsaturated flow in poroelastic media and nonlinear transport can also be studied, using for example techniques developed in Both et al. (2018) and Radu et al. (2010).

The rest of the paper is organized as follows. The coupled Stokes–Darcy-transport problem and its variational formulation are presented in Sect. 2. The semi-discrete continuous-in-time approximation is developed in Sect. 3 and analyzed in Sect. 4. Computational experiments confirming the convergence of the method and illustrating its performance for a range of applications of flow in fractured poroelastic media are presented in Sect. 5.

2 Model problem

We consider a simulation domain $\Omega \subset \mathbb{R}^d$, $d = 2, 3$ which is a union of non-overlapping and possibly non-connected regions Ω_f and Ω_p, where Ω_f is a fracture region and Ω_p is a poroelasticity region, see Fig. 1. We denote by $\Gamma_{fp} = \partial\Omega_f \cap \partial\Omega_p$ the interface between Ω_f and Ω_p. We further denote by $(\mathbf{u}_\star, p_\star)$ the velocity-pressure

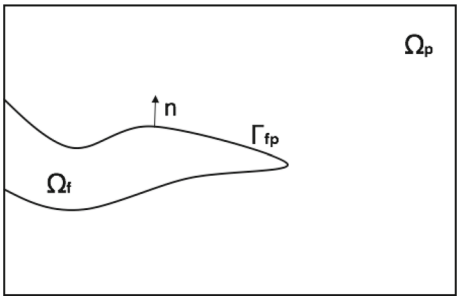

Fig. 1 Schematic representation of the physical domain

pairs in $\Omega_\star$, $\star = f, p$, by $\boldsymbol{\eta}_p$ the displacement in Ω_p and by $(\mathbf{f}_\star, q_\star)$ the body force and the external source or sink terms. The flow in the fracture region Ω_f is governed by the Stokes equations

$$-\nabla \cdot \boldsymbol{\sigma}_f(\mathbf{u}_f, p_f) = \mathbf{f}_f \qquad \text{in } \Omega_f \times (0, T], \tag{2.1}$$

$$\nabla \cdot \mathbf{u}_f = q_f \qquad \text{in } \Omega_f \times (0, T], \tag{2.2}$$

where the deformation and stress tensors, $\boldsymbol{\epsilon}(\mathbf{u})$ and $\boldsymbol{\sigma}_f(\mathbf{u}_f, p_f)$, are given by

$$\boldsymbol{\epsilon}(\mathbf{u}) = \frac{1}{2}\left(\nabla \mathbf{u}_f + \nabla \mathbf{u}_f^T\right), \quad \boldsymbol{\sigma}_f(\mathbf{u}_f, p_f) = -p_f \mathbf{I} + 2\nu \boldsymbol{\epsilon}(\mathbf{u}_f),$$

and ν denotes the fluid viscosity.

Let $\boldsymbol{\sigma}_e(\boldsymbol{\eta})$ and $\boldsymbol{\sigma}_p(\boldsymbol{\eta}, p)$ be the elasticity and poroelasticity stress tensors, respectively:

$$\boldsymbol{\sigma}_e(\boldsymbol{\eta}) = \lambda_p(\nabla \cdot \boldsymbol{\eta})\mathbf{I} + 2\mu_p \boldsymbol{\epsilon}(\boldsymbol{\eta}), \quad \boldsymbol{\sigma}_p(\boldsymbol{\eta}, p) = \boldsymbol{\sigma}_e(\boldsymbol{\eta}) - \alpha p_p \mathbf{I},$$

where α_p is the Biot–Willis constant and λ_p, μ_p are the Lamé coefficients.

The poroelasticity region Ω_p is governed by the quasi-static Biot system (Biot 1941)

$$-\nabla \cdot \boldsymbol{\sigma}_p(\boldsymbol{\eta}_p, p_p) = \mathbf{f}_p, \quad \nu K^{-1}\mathbf{u}_p + \nabla p_p = 0 \qquad \text{in } \Omega_p \times (0, T], \tag{2.3}$$

$$\frac{\partial}{\partial t}(s_0 p_p + \alpha \nabla \cdot \boldsymbol{\eta}_p) + \nabla \cdot \mathbf{u}_p = q_p \qquad \text{in } \Omega_p \times (0, T], \tag{2.4}$$

where s_0 is a storage coefficient and K is a symmetric and uniformly positive definite permeability tensor.

Following Ambartsumyan et al. (2018b), Badia et al. (2009), and Showalter (2005), on the fluid–poroelasticity interface Γ_{fp} we prescribe the following *interface conditions*: *mass conservation*, *balance of normal stress*, *conservation of momentum*, and the Beavers–Joseph–Saffman (BJS) condition modeling *slip with friction* (Beavers and Joseph 1967; Saffman 1971):

$$\mathbf{u}_f \cdot \mathbf{n}_f + \left(\frac{\partial \boldsymbol{\eta}_p}{\partial t} + \mathbf{u}_p\right) \cdot \mathbf{n}_p = 0 \qquad \text{on } \Gamma_{fp} \times (0, T], \tag{2.5}$$

$$-(\boldsymbol{\sigma}_f \mathbf{n}_f)\cdot\mathbf{n}_f = p_p, \qquad \boldsymbol{\sigma}_f \mathbf{n}_f + \boldsymbol{\sigma}_p \mathbf{n}_p = 0 \qquad \text{on } \Gamma_{fp}\times(0,T], \quad (2.6)$$

$$-(\boldsymbol{\sigma}_f \mathbf{n}_f)\cdot\boldsymbol{\tau}_{f,j} = \nu\alpha_{BJS}\sqrt{K_j^{-1}}\left(\mathbf{u}_f - \frac{\partial\boldsymbol{\eta}_p}{\partial t}\right)\cdot\boldsymbol{\tau}_{f,j} \qquad \text{on } \Gamma_{fp}\times(0,T], \quad (2.7)$$

where $\mathbf{n}_f$ and $\mathbf{n}_p$ are the outward unit normal vectors to $\partial\Omega_f$ and $\partial\Omega_p$, respectively, $\boldsymbol{\tau}_{f,j}$, $1 \le j \le d-1$, is an orthogonal system of unit tangent vectors on Γ_{fp}, $K_j = (K\boldsymbol{\tau}_{f,j})\cdot\boldsymbol{\tau}_{f,j}$ and $\alpha_{BJS} > 0$ is an experimentally determined friction coefficient.

The above system of equations is complemented by a set of boundary and initial conditions. Let $\Gamma_f = \partial\Omega_f\backslash\Gamma_{fp}$, $\Gamma_p = \partial\Omega_p\backslash\Gamma_{fp} = \Gamma_p^N \cup \Gamma_p^D$. For simplicity we assume homogeneous boundary conditions

$$\mathbf{u}_f = 0 \text{ on } \Gamma_f\times(0,T], \quad \mathbf{u}_p\cdot\mathbf{n}_p = 0 \text{ on } \Gamma_p^N\times(0,T], \quad p_p = 0 \text{ on } \Gamma_p^D\times(0,T],$$
$$\boldsymbol{\eta}_p = 0 \text{ on } \Gamma_p\times(0,T].$$

We further set the initial conditions

$$p_p(\mathbf{x},0) = p_{p,0}(\mathbf{x}), \ \ \boldsymbol{\eta}_p(\mathbf{x},0) = \boldsymbol{\eta}_{p,0}(\mathbf{x}) \text{ in } \Omega_p.$$

Throughout the paper we will use the following standard notation. For a domain $G \subset \mathbb{R}^d$, the $L^2(G)$ inner product and norm for scalar and vector valued functions are denoted by $(\cdot,\cdot)_G$ and $\|\cdot\|_G$, respectively. The norms and seminorms of the Sobolev spaces $W^{k,p}(G)$, $k \in \mathbb{R}$, $p > 0$ are denoted by $\|\cdot\|_{k,p,G}$ and $|\cdot|_{k,p,G}$, respectively. Conventionally, the norms and seminorms of Hilbert spaces $H^k(G)$ are denoted by $\|\cdot\|_{k,G}$ and $|\cdot|_{k,G}$, respectively. For a section of the domain or element boundary $S \subset \mathbb{R}^{d-1}$ we write $\langle\cdot,\cdot\rangle_S$ and $\|\cdot\|_S$ for the $L^2(S)$ inner product (or duality pairing) and norm, respectively. We will also use the space

$$H(\mathrm{div};G) = \{\mathbf{v} \in L^2(G) : \nabla\cdot\mathbf{v} \in L^2(G)\}$$

equipped with the norm

$$\|\mathbf{v}\|_{\mathrm{div},G} = \left(\|\mathbf{v}\|^2 + \|\nabla\cdot\mathbf{v}\|^2\right)^{1/2}.$$

For the weak formulation of the coupled Stokes–Biot equations we introduce the following function spaces:

$$\mathbf{V}_f = \{\mathbf{v}_f \in H^1(\Omega_f)^d : \mathbf{v}_f = 0 \text{ on } \Gamma_f\}, \qquad W_f = L^2(\Omega_f), \quad (2.8)$$

$$\mathbf{V}_p = \{\mathbf{v}_p \in H(\mathrm{div};\Omega_p) : \mathbf{v}_p\cdot\mathbf{n}_p = 0 \text{ on } \Gamma_p^N\}, \qquad W_p = L^2(\Omega_p), \quad (2.9)$$

$$\mathbf{X}_p = \{\boldsymbol{\xi}_p \in H^1(\Omega_p)^d : \boldsymbol{\xi}_p = 0 \text{ on } \Gamma_p\}, \quad (2.10)$$

equipped with the norms

$$\|\mathbf{v}_f\|_{\mathbf{V}_f} = \|\mathbf{v}_f\|_{1,\Omega_f}, \qquad \|w_f\|_{W_f} = \|w_f\|_{\Omega_f},$$
$$\|\mathbf{v}_p\|_{\mathbf{V}_p} = \|\mathbf{v}_p\|_{\mathrm{div},\Omega_p}, \qquad \|w_p\|_{W_p} = \|w_p\|_{\Omega_p},$$

$$\|\boldsymbol{\eta}_p\|_{\mathbf{X}_p} = \|\boldsymbol{\eta}_p\|_{1,\Omega_p}.$$

The weak formulation is obtained by multiplying the equations in each region by the corresponding test functions, integrating by parts the second order terms in space, and utilizing the interface and boundary conditions. The integration by parts in (2.1) and (2.3) leads to the bilinear forms, corresponding to the Stokes, Darcy and the elasticity operators:

$$\begin{aligned}
&a_f(\cdot,\cdot) : \mathbf{V}_f \times \mathbf{V}_f \longrightarrow \mathbb{R}, \qquad a_f(\mathbf{u}_f, \mathbf{v}_f) := (2\nu\boldsymbol{\epsilon}(\mathbf{u}_f), \boldsymbol{\epsilon}(\mathbf{v}_f))_{\Omega_f},\\
&a_p^d(\cdot,\cdot) : \mathbf{V}_p \times \mathbf{V}_p \longrightarrow \mathbb{R}, \qquad a_p^d(\mathbf{u}_p, \mathbf{v}_p) := (\nu K^{-1}\mathbf{u}_p, \mathbf{v}_p)_{\Omega_p},\\
&a_p^e(\cdot,\cdot) : \mathbf{X}_p \times \mathbf{X}_p \longrightarrow \mathbb{R}, \qquad a_p^e(\boldsymbol{\eta}_p, \boldsymbol{\xi}_p) := (2\mu_p\boldsymbol{\epsilon}(\boldsymbol{\eta}_p), \boldsymbol{\epsilon}(\boldsymbol{\xi}_p))_{\Omega_p}\\
&\quad + (\lambda_p \nabla\cdot\boldsymbol{\eta}_p, \nabla\cdot\boldsymbol{\xi}_p)_{\Omega_p},
\end{aligned}$$

the bilinear forms

$$b_\star(\cdot,\cdot) : \mathbf{V}_\star \times W_\star \longrightarrow \mathbb{R}, \qquad b_\star(\mathbf{v}, w) := -(\nabla\cdot\mathbf{v}, w)_{\Omega_\star}, \quad \star = f, p,$$

and the interface term

$$I_{\Gamma_{fp}} = -\langle\boldsymbol{\sigma}_f\mathbf{n}_f, \mathbf{v}_f\rangle_{\Gamma_{fp}} - \langle\boldsymbol{\sigma}_p\mathbf{n}_p, \boldsymbol{\xi}_p\rangle_{\Gamma_{fp}} + \langle p_p, \mathbf{v}_p\cdot\mathbf{n}_p\rangle_{\Gamma_{fp}}.$$

To handle the interface term, we introduce a Lagrange multiplier λ with a meaning of Darcy pressure on the interface (Ambartsumyan et al. 2018b)

$$\lambda = -(\boldsymbol{\sigma}_f\mathbf{n}_f)\cdot\mathbf{n}_f = p_p \quad \text{on } \Gamma_{fp}.$$

Using (2.6)–(2.7), we obtain

$$I_{\Gamma_{fp}} = a_{BJS}(\mathbf{u}_f, \partial_t\boldsymbol{\eta}_p; \mathbf{v}_f, \boldsymbol{\xi}_p) + b_\Gamma(\mathbf{v}_f, \mathbf{v}_p, \boldsymbol{\xi}_p; \lambda),$$

where

$$\begin{aligned}
a_{BJS}(\mathbf{u}_f, \boldsymbol{\eta}_p; \mathbf{v}_f, \boldsymbol{\xi}_p) &= \sum_{j=1}^{d-1} \left\langle \nu_I\, \alpha_{BJS}\sqrt{K^{-1}}(\mathbf{u}_f - \boldsymbol{\eta}_p)\cdot\boldsymbol{\tau}_{f,j}, (\mathbf{v}_f - \boldsymbol{\xi}_p)\cdot\boldsymbol{\tau}_{f,j}\right\rangle_{\Gamma_{fp}},\\
b_\Gamma(\mathbf{v}_f, \mathbf{v}_p, \boldsymbol{\xi}_p; \mu) &= \langle\mathbf{v}_f\cdot\mathbf{n}_f + (\boldsymbol{\xi}_p + \mathbf{v}_p)\cdot\mathbf{n}_p, \mu\rangle_{\Gamma_{fp}}.
\end{aligned}$$

We note that for the well-posedness of b_Γ term, we require $\lambda \in (\mathbf{V}_p\cdot\mathbf{n}_p|_{\Gamma_{fp}})'$. The normal trace theorem for $\mathbf{v}_p \in \mathbf{V}_p \subset H(\mathrm{div};\Omega_p)$ implies that $\mathbf{v}_p\cdot\mathbf{n}_p \in H^{-1/2}(\partial\Omega_p)$. With our choice of boundary conditions, one can verify that $\mathbf{v}_p\cdot\mathbf{n}_p \in H^{-1/2}(\Gamma_{fp})$, see Ambartsumyan et al. (2018b). Therefore, we take $\Lambda = H^{1/2}(\Gamma_{fp})$.

Stokes–Biot variational formulation: given $p_p(0) = p_{p,0} \in W_p$, $\boldsymbol{\eta}_p(0) = \boldsymbol{\eta}_{p,0} \in \mathbf{X}_p$, find, for $t \in (0,T]$, $\mathbf{u}_f(t) \in \mathbf{V}_f$, $p_f(t) \in W_f$, $\mathbf{u}_p(t) \in \mathbf{V}_p$, $p_p(t) \in W_p$,

$\boldsymbol{\eta}_p(t) \in \mathbf{X}_p$, and $\lambda(t) \in \Lambda$ such that for all $\mathbf{v}_f \in \mathbf{V}_f$, $w_f \in W_f$, $\mathbf{v}_p \in \mathbf{V}_p$, $w_p \in W_p$, $\boldsymbol{\xi}_p \in \mathbf{X}_p$, and $\mu \in \Lambda$,

$$\begin{aligned} &a_f(\mathbf{u}_f, \mathbf{v}_f) + a_p^d(\mathbf{u}_p, \mathbf{v}_p) + a_p^e(\boldsymbol{\eta}_p, \boldsymbol{\xi}_p) + a_{BJS}(\mathbf{u}_f, \partial_t \boldsymbol{\eta}_p; \mathbf{v}_f, \boldsymbol{\xi}_p) \\ &\quad + b_f(\mathbf{v}_f, p_f) + b_p(\mathbf{v}_p, p_p) + \alpha_p b_p(\boldsymbol{\xi}_p, p_p) \\ &\quad + b_\Gamma(\mathbf{v}_f, \mathbf{v}_p, \boldsymbol{\xi}_p; \lambda) = (\mathbf{f}_f, \mathbf{v}_f)_{\Omega_f} + (\mathbf{f}_p, \boldsymbol{\xi}_p)_{\Omega_p}, \end{aligned} \tag{2.11}$$

$$\begin{aligned} &\left(s_0 \partial_t p_p, w_p\right)_{\Omega_p} - \alpha_p b_p\left(\partial_t \boldsymbol{\eta}_p, w_p\right) - b_p(\mathbf{u}_p, w_p) - b_f(\mathbf{u}_f, w_f) \\ &\quad = (q_f, w_f)_{\Omega_f} + (q_p, w_p)_{\Omega_p}, \end{aligned} \tag{2.12}$$

$$b_\Gamma\left(\mathbf{u}_f, \mathbf{u}_p, \partial_t \boldsymbol{\eta}_p; \mu\right) = 0. \tag{2.13}$$

The well-posedness of the above problem has been established in Ambartsumyan et al. (2018a).

Theorem 2.1 *For each* $\mathbf{f}_f \in W^{1,1}(0, T; \mathbf{V}_f')$, $\mathbf{f}_p \in W^{1,1}(0, T; \mathbf{X}_p')$, $q_f \in W^{1,1}(0, T; W_f')$, $q_p \in W^{1,1}(0, T; W_p')$, *and* $p_p(0) = p_{p,0} \in W_p$, $\boldsymbol{\eta}_p(0) = \boldsymbol{\eta}_{p,0} \in \mathbf{X}_p$, *there exists a unique solution* $(\mathbf{u}_f(t), p_f(t), \mathbf{u}_p(t), p_p(t), \boldsymbol{\eta}_p(t), \lambda(t)) \in L^\infty(0, T; \mathbf{V}_f) \times L^\infty(0, T; W_f) \times L^\infty(0, T; \mathbf{V}_p) \times W^{1,\infty}(0, T; W_p) \times W^{1,\infty}(0, T; \mathbf{X}_p) \times L^\infty(0, T; \Lambda)$ *of* (2.11)–(2.13).

The Stokes–Biot problem is coupled with the transport equation in Ω:

$$\phi c_t + \nabla \cdot (c\mathbf{u} - \mathbf{D}\nabla c) = q\tilde{c}, \quad \text{in } \Omega \times (0, T], \tag{2.14}$$

where $c(\mathbf{x}, t)$ is the concentration of some chemical component, $0 < \phi_* \le \phi(\mathbf{x}) \le \phi^*$ is the porosity of the medium in Ω_p (it is set to 1 in Ω_f), $\mathbf{u}$ is the velocity field over $\Omega = \Omega_f \cup \Omega_p$, defined as $\mathbf{u}|_{\Omega_f} = \mathbf{u}_f, \mathbf{u}|_{\Omega_p} = \mathbf{u}_p$, q is the source term given by $q\big|_{\Omega_f} = q_f$ and $q\big|_{\Omega_p} = q_p$, and

$$\tilde{c} = \begin{cases} \text{injected concentration } c_w, & q > 0, \\ \text{resident concentration } c, & q < 0. \end{cases}$$

The diffusion/dispersion tensor $\mathbf{D}$, which combines the effects of molecular diffusion and mechanical dispersion, is a nonlinear function of the velocity, given by (Peaceman 1977)

$$\mathbf{D}(\mathbf{u}) = d_m \mathbf{I} + |\mathbf{u}|\{\alpha_l \mathbf{E}(\mathbf{u}) + \alpha_t(\mathbf{I} - \mathbf{E}(\mathbf{u}))\}, \tag{2.15}$$

where $d_m = \phi\tau D_m$, τ is the tortuosity coefficient, D_m is the molecular diffusivity, $\mathbf{E}(\mathbf{u})$ is the tensor that projects onto the $\mathbf{u}$ direction with $(\mathbf{E}(\mathbf{u}))_{ij} = \frac{u_i u_j}{|\mathbf{u}|^2}$, and α_l, α_t are the longitudinal and transverse dispersion, respectively.

The model is complemented by the initial condition

$$c(\mathbf{x}, 0) = c_0(\mathbf{x}) \quad \text{in } \Omega, \tag{2.16}$$

and the boundary conditions

$$(c\mathbf{u} - \mathbf{D}\nabla c) \cdot \mathbf{n} = (c_{in}\mathbf{u}) \cdot \mathbf{n} \qquad \text{on } \Gamma_{in} \times (0, T], \tag{2.17}$$

$$(\mathbf{D}\nabla c) \cdot \mathbf{n} = 0 \qquad \text{on } \Gamma_{out} \times (0, T], \tag{2.18}$$

where $\Gamma_{in} := \{\mathbf{x} \in \partial\Omega : \mathbf{u} \cdot \mathbf{n} < 0\}$, $\Gamma_{out} := \{\mathbf{x} \in \partial\Omega : \mathbf{u} \cdot \mathbf{n} \geq 0\}$ and $\mathbf{n}$ is the unit outward normal vector to $\partial\Omega$.

Remark 2.1 We note that the coupling between the flow and transport problems is one way. In particular, the transport equation uses the Stokes–Biot velocity, but the flow problem does not depend on the concentration.

3 Semi-discrete continuous-in-time formulation

Let $\mathcal{T}_h^f$ and $\mathcal{T}_h^p$ be shape-regular and quasi-uniform affine element partitions of Ω_f and Ω_p (Ciarlet 2002), respectively, both consisting of elements with maximal element diameter h. The two partitions may be non-matching at the interface Γ_{fp}. We also consider a shape-regular and quasi-uniform affine element partition of Ω, denoted by $\mathcal{T}_h$. We note that $\mathcal{T}_h$ may be different from $\mathcal{T}_h^f$ and $\mathcal{T}_h^p$. We denote by E_h the set of all interior facets of $\mathcal{T}_h$ and on each facet we arbitrarily fix a unit normal vector $\mathbf{n}_e$. We further denote E_h^{out} and E_h^{in} the set of facets on Γ_{out} and Γ_{in}, for which $\mathbf{n}_e$ coincides with the outward unit normal vector.

For the discretization of the fluid velocity and pressure we choose finite element spaces $\mathbf{V}_{f,h} \subset \mathbf{V}_f$ and $W_{f,h} \subset W_f$, which are assumed to be inf-sup stable. Examples of such spaces include the MINI elements, the Taylor–Hood elements and the conforming Crouzeix–Raviart elements (Boffi et al. 2013). For the discretization of the porous medium problem we choose $\mathbf{V}_{p,h} \subset \mathbf{V}_p$ and $W_{p,h} \subset W_p$ to be any inf-sup stable mixed finite element spaces, such as the Raviart-Thomas or the Brezzi–Douglas–Marini spaces (Boffi et al. 2013). We employ a conforming Lagrange finite element space $\mathbf{X}_{p,h} \subset \mathbf{X}_p$ to approximate the structure displacement. For the discretization of the Lagrange multiplier variable we set

$$\Lambda_h = \mathbf{V}_{p,h} \cdot \mathbf{n}_p|_{\Gamma_{fp}},$$

which allows for optimal order approximation on non-matching grids (Layton et al. 2003). We note that this is a non-conforming choice, since $\Lambda_h \not\subset H^{1/2}(\Gamma_{fp})$. The space is equipped with the discrete $H^{1/2}$-norm analogue, $\|\mu_h\|_{\Lambda_h}^2 = \|\mu_h\|_{\Gamma_{fp}}^2 + |\mu_h|_{\Lambda_h}^2$ (Ambartsumyan et al. 2018b; Galvis and Sarkis 2007) with the semi-norm

$$|\mu_h|_{\Lambda_h}^2 = a_p^d(\mathbf{u}_{p,h}^*(\mu_h), \mathbf{u}_{p,h}^*(\mu_h)), \tag{3.1}$$

where $(\mathbf{u}_{p,h}^*(\mu_h), p_{p,h}^*(\mu_h)) \in \mathbf{V}_{p,h} \times W_{p,h}$ is the mixed finite element solution to the Darcy problem with Dirichlet data μ_h on Γ_{fp}:

$$a_p^d(\mathbf{u}_{p,h}^*(\mu_h), \mathbf{v}_{p,h}) + b_p(\mathbf{v}_{p,h}, p_h^*(\mu_h)) = -\langle \mathbf{v}_{p,h} \cdot \mathbf{n}_p, \mu_h \rangle_{\Gamma_{fp}}, \quad \forall\, \mathbf{v}_{p,h} \in \mathbf{V}_{p,h},$$

$$b_p(\mathbf{u}^*_{p,h}(\mu_h), w_{p,h}) = 0, \quad \forall\, w_{p,h} \in W_{p,h}.$$

We denote by $k_f \geq 1$ and $s_f \geq 1$ the degrees of polynomials in the spaces $\mathbf{V}_{f,h}$ and $W_{f,h}$ respectively. Let $k_p \geq 0$ and $s_p \geq 0$ be the degrees of polynomials in the spaces $\mathbf{V}_{p,h}$ and $W_{p,h}$ respectively. Finally, let $k_s \geq 1$ be the polynomial degree in $\mathbf{X}_{p,h}$.

Semi-discrete Stokes–Biot problem: given $p_{p,h}(0)$ and $\boldsymbol{\eta}_{p,h}(0)$, for $t \in (0, T]$, find $\mathbf{u}_{f,h}(t) \in \mathbf{V}_{f,h}$, $p_{f,h}(t) \in W_{f,h}$, $\mathbf{u}_{p,h}(t) \in \mathbf{V}_{p,h}$, $p_{p,h}(t) \in W_{p,h}$, $\boldsymbol{\eta}_{p,h}(t) \in \mathbf{X}_{p,h}$, and $\lambda_h(t) \in \Lambda_h$ such that for all $\mathbf{v}_{f,h} \in \mathbf{V}_{f,h}$, $w_{f,h} \in W_{f,h}$, $\mathbf{v}_{p,h} \in \mathbf{V}_{p,h}$, $w_{p,h} \in W_{p,h}$, $\boldsymbol{\xi}_{p,h} \in \mathbf{X}_{p,h}$, and $\mu_h \in \Lambda_h$,

$$\begin{aligned}
&a_f(\mathbf{u}_{f,h}, \mathbf{v}_{f,h}) + a_p^d(\mathbf{u}_{p,h}, \mathbf{v}_{p,h}) + a_p^e(\boldsymbol{\eta}_{p,h}, \boldsymbol{\xi}_{p,h}) + a_{BJS}(\mathbf{u}_{f,h}, \partial_t \boldsymbol{\eta}_{p,h}; \mathbf{v}_{f,h}, \boldsymbol{\xi}_{p,h}) \\
&\quad + b_f(\mathbf{v}_{f,h}, p_{f,h}) + b_p(\mathbf{v}_{p,h}, p_{p,h}) + \alpha b_p(\boldsymbol{\xi}_{p,h}, p_{p,h}) \\
&\quad + b_\Gamma(\mathbf{v}_{f,h}, \mathbf{v}_{p,h}, \boldsymbol{\xi}_{p,h}; \lambda_h) = (\mathbf{f}_f, \mathbf{v}_{f,h})_{\Omega_f} + (\mathbf{f}_p, \boldsymbol{\xi}_{p,h})_{\Omega_p}, \qquad (3.2) \\
&(s_0 \partial_t p_{p,h}, w_{p,h})_{\Omega_p} - \alpha b_p(\partial_t \boldsymbol{\eta}_{p,h}, w_{p,h}) - b_p(\mathbf{u}_{p,h}, w_{p,h}) - b_f(\mathbf{u}_{f,h}, w_{f,h}) \\
&\quad = (q_f, w_{f,h})_{\Omega_f} + (q_p, w_{p,h})_{\Omega_p}, \qquad (3.3) \\
&b_\Gamma(\mathbf{u}_{f,h}, \mathbf{u}_{p,h}, \partial_t \boldsymbol{\eta}_{p,h}; \mu_h) = 0. \qquad (3.4)
\end{aligned}$$

We take $p_{p,h}(0) = Q_{p,h} p_{p,0}$ and $\boldsymbol{\eta}_{p,h}(0) = I_{s,h} \boldsymbol{\eta}_{p,0}$, where the operators $Q_{p,h}$ and $I_{s,h}$ are defined in Sect. 4.

It was shown in Ambartsumyan et al. (2018b) that the above problem has a unique solution satisfying

$$\begin{aligned}
&\|\boldsymbol{\eta}_p - \boldsymbol{\eta}_{p,h}\|_{L^\infty(0,T;H^1(\Omega_p))} + \sqrt{s_0}\|p_p - p_{p,h}\|_{L^\infty(0,T;L^2(\Omega_p))} \\
&\quad + \|\mathbf{u}_f - \mathbf{u}_{f,h}\|_{L^2(0,T;H^1(\Omega_f))} + \|\mathbf{u}_p - \mathbf{u}_{p,h}\|_{L^2(0,T;L^2(\Omega_p))} \\
&\quad + \left|(\mathbf{u}_f - \partial_t \boldsymbol{\eta}_p) - (\mathbf{u}_{f,h} - \partial_t \boldsymbol{\eta}_{p,h})\right|_{L^2(0,T;a_{BJS})} \\
&\quad + \|p_f - p_{f,h}\|_{L^2(0,T;L^2(\Omega_f))} + \|p_p - p_{p,h}\|_{L^2(0,T;L^2(\Omega_p))} + \|\lambda - \lambda_h\|_{L^2(0,T;\Lambda_h)} \\
&\leq C\Big(h^{r_{k_f}} \|\mathbf{u}_f\|_{L^2(0,T;H^{r_{k_f}+1}(\Omega_f))} \\
&\quad + h^{r_{s_f}} \|p_f\|_{L^2(0,T;H^{r_{s_f}}(\Omega_f))} + h^{r_{k_p}} \|\mathbf{u}_p\|_{L^2(0,T;H^{r_{k_p}}(\Omega_p))} \\
&\quad + h^{\tilde{r}_{k_p}} \left(\|\lambda\|_{L^2(0,T;H^{\tilde{r}_{k_p}}(\Gamma_{fp}))} + \|\lambda\|_{L^\infty(0,T;H^{\tilde{r}_{k_p}}(\Gamma_{fp}))} + \|\partial_t \lambda\|_{L^2(0,T;H^{\tilde{r}_{k_p}}(\Gamma_{fp}))} \right) \\
&\quad + h^{r_{s_p}} \left(\|p_p\|_{L^\infty(0,T;H^{r_{s_p}}(\Omega_p))} + \|p_p\|_{L^2(0,T;H^{r_{s_p}}(\Omega_p))} + \|\partial_t p_p\|_{L^2(0,T;H^{r_{s_p}}(\Omega_p))} \right) \\
&\quad + h^{r_{k_s}} \Big(\|\boldsymbol{\eta}_p\|_{L^\infty(0,T;H^{r_{k_s}+1}(\Omega_p))} + \|\boldsymbol{\eta}_p\|_{L^2(0,T;H^{r_{k_s}+1}(\Omega_p))} \\
&\quad + \|\partial_t \boldsymbol{\eta}_p\|_{L^2(0,T;H^{r_{k_s}+1}(\Omega_p))} \Big) \Big), \\
&0 \leq r_{k_f} \leq k_f, \ 0 \leq r_{s_f} \leq s_f + 1, \ 1 \leq \{r_{k_p}, \tilde{r}_{k_p}\} \leq k_p + 1, \\
&0 \leq r_{s_p} \leq s_p + 1, \ 0 \leq r_{k_s} \leq k_s, \qquad (3.5)
\end{aligned}$$

where, for $\mathbf{v}_f \in \mathbf{V}_f$, $\boldsymbol{\xi}_p \in \mathbf{X}_p$,

$$|\mathbf{v}_f - \boldsymbol{\xi}_p|^2_{a_{BJS}} = a_{BJS}(\mathbf{v}_f, \boldsymbol{\xi}_p; \mathbf{v}_f, \boldsymbol{\xi}_p) = \sum_{j=1}^{d-1} \mu\alpha_{BJS} \| K_j^{-1/4}(\mathbf{v}_f - \boldsymbol{\xi}_p) \cdot \boldsymbol{\tau}_{f,j} \|^2_{L^2(\Gamma_{fp})}.$$

We note that the result was derived under the assumption $|\Gamma_p^D| \neq 0$, but can be extended to the case of full Neumann boundary condition on Γ_p by restricting the mean value of the pressure over the entire domain to be zero.

Next, we derive the numerical method for the transport problem. Following Sun et al. (2002), we adopt the DG scheme known as the non-symmetric interior penalty Galerkin (NIPG) (Rivière et al. 1999).

For $s \geq 0$, we define the space

$$H^s(\mathcal{T}_h) = \{\phi \in L^2(\Omega) : \phi \in H^s(E), E \in \mathcal{T}_h\}.$$

The jump and average for $\phi \in H^s(\mathcal{T}_h)$, $s > 1/2$ are defined as follows. Let $E_i, E_j \in \mathcal{T}_h$ and $e = \partial E_i \cap \partial E_j \in E_h$, with $\mathbf{n}_e$ exterior to E_i. Let

$$[\phi] = (\phi|_{E_i})|_e - (\phi|_{E_j})|_e, \quad \{\phi\} = \frac{(\phi|_{E_i})|_e + (\phi|_{E_j})|_e}{2}.$$

For $\phi \in H^1(\mathcal{T}_h)$ we define the broken seminorm

$$|||\nabla\phi|||_\Omega = \left(\sum_{E \in \mathcal{T}_h} \|\nabla\phi\|^2_E \right)^{1/2}.$$

We consider the finite element space

$$\mathcal{D}_r(\mathcal{T}_h) = \{\phi \in L^2(\Omega) : \phi|_E \in \mathcal{P}_r(E), E \in \mathcal{T}_h\},$$

where $\mathcal{P}_r(E)$ denotes the space of polynomials of degree less than or equal to r on E.

Let the bilinear form $B_{\mathbf{u}_h}(c_h, \psi_h)$ and the linear functional $L_h(\psi_h)$ be defined as follows:

$$\begin{aligned} B_{\mathbf{u}_h}(c_h, \psi_h) &= \sum_{E \in \mathcal{T}_h} \int_E (\mathbf{D}(\mathbf{u}_h)\nabla c_h - c_h\mathbf{u}_h) \cdot \nabla\psi_h - \sum_{e \in E_h} \int_e \{\mathbf{D}(\mathbf{u}_h)\nabla c_h \cdot \mathbf{n}_e\}[\psi_h] \\ &\quad + \sum_{e \in E_h} \int_e \{\mathbf{D}(\mathbf{u}_h)\nabla\psi_h \cdot \mathbf{n}_e\}[c_h] + \sum_{e \in E_h} \int_e c_h^* \mathbf{u}_h \cdot \mathbf{n}_e [\psi_h] \end{aligned}$$

$$+ \sum_{e \in E_h^{out}} \int_e c_h \mathbf{u}_h \cdot \mathbf{n}_e \psi_h - \int_\Omega c_h q^- \psi_h + J_0^\sigma(c_h, \psi_h),$$

$$L_h(\psi_h) = \int_\Omega c_w q^+ \psi_h - \sum_{e \in E_h^{in}} \int_e c_{in} \mathbf{u}_h \cdot \mathbf{n}_e \psi_h. \tag{3.6}$$

Here $q^+ = \max(q, 0)$ is the injection part of the source term and $q^- = \min(q, 0)$ is the extraction part, $c_h^*|_e$ is the upwind value of concentration, defined as

$$c_h^*|_e = \begin{cases} c_h|_{E_1} & \text{if } \mathbf{u}_h \cdot \mathbf{n}_e > 0, \\ c_h|_{E_2} & \text{if } \mathbf{u}_h \cdot \mathbf{n}_e < 0, \end{cases} \tag{3.7}$$

and $J_0^\sigma(c_h, \psi_h)$ is the interior penalty term

$$J_0^\sigma(c_h, \psi_h) = \sum_{e \in E_h} \frac{\sigma_e}{h_e} \int_e [c_h][\psi_h], \tag{3.8}$$

where, σ is a discrete positive function that takes constant value σ_e on the edge and is bounded below by $\sigma_* > 0$ and above by σ^*, and h_e is the diameter of side of facet e.

Semi-discrete DG transport problem: find $c_h(t) \in \mathcal{D}_r(\mathcal{T}_h)$ such that $\forall \psi_h \in \mathcal{D}_r(\mathcal{T}_h)$,

$$(\phi \partial_t c_h, \psi_h) + B_{\mathbf{u}_h}(c_h, \psi_h) = L_h(\psi_h), \tag{3.9}$$

with initial condition $c_h(0)$ a suitable approximation of c_0.

It is easy to verify that, if the solution to (2.14) is sufficiently regular, it satisfies (3.9) with $B_{\mathbf{u}_h}$ replaced by $B_{\mathbf{u}}$.

4 Analysis of the semi-discrete problem

In this section we discuss the stability and error estimates for the transport problem (3.9). We note that a similar scheme has been used and analyzed in details in Sun et al. (2002). The main difference and improvement in this work is the fact that the numerically computed velocity field $\mathbf{u}_h$ is directly incorporated into the scheme for transport (3.9), while Sun et al. (2002) used a cut-off operator in order to ensure stability of their method. We avoid the need for a cut-off operator by establishing pointwise stability of the velocity solution in space and time, which is done in the next two lemmas. We first establish an error estimate for the fluid velocity in $L^\infty(0, T)$. The result requires control of $\mathbf{u}_{f,h}(0)$ and $\mathbf{u}_{p,h}(0)$. To simplify the analysis, we assume that the initial pressure $p_{p,0}$ and displacement $\boldsymbol{\eta}_{p,0}$ are constants.

Lemma 4.1 *Assume that $p_{p,0}$ and $\boldsymbol{\eta}_{p,0}$ are constants. If the solution of (2.11)–(2.13) is sufficiently regular, there exists a positive constant C independent of h such that*

$$
\begin{aligned}
&\|\mathbf{u}_f - \mathbf{u}_{f,h}\|_{L^\infty(0,T;H^1(\Omega_f))} + \|\mathbf{u}_p - \mathbf{u}_{p,h}\|_{L^\infty(0,T;L^2(\Omega_p))} \\
&\le C\Big[h^{r_{k_f}}\left(\|\mathbf{u}_f\|_{L^2(0,T;H^{r_{k_f}+1}(\Omega_f))} + \|\mathbf{u}_f\|_{L^\infty(0,T;H^{r_{k_f}+1}(\Omega_f))} + \|\partial_t \mathbf{u}_f\|_{L^2(0,T;H^{r_{k_f}+1}(\Omega_f))}\right) \\
&\quad + h^{r_{s_f}}\left(\|p_f\|_{L^2(0,T;H^{r_{s_f}}(\Omega_f))} + \|p_f\|_{L^\infty(0,T;H^{r_{s_f}}(\Omega_f))} + \|\partial_t p_f\|_{L^2(0,T;H^{r_{s_f}}(\Omega_f))}\right) \\
&\quad + h^{r_{k_p}}\left(\|\mathbf{u}_p\|_{L^2(0,T;H^{r_{k_p}}(\Omega_p))} + \|\mathbf{u}_p\|_{L^\infty(0,T;H^{r_{k_p}}(\Omega_p))} + \|\partial_t \mathbf{u}_p\|_{L^2(0,T;H^{r_{k_p}}(\Omega_p))}\right) \\
&\quad + h^{\tilde{r}_{k_p}}\left(\|\lambda\|_{L^2(0,T;H^{\tilde{r}_{k_p}}(\Gamma_{fp}))} + \|\lambda\|_{L^\infty(0,T;H^{\tilde{r}_{k_p}}(\Gamma_{fp}))} + \|\partial_t \lambda\|_{L^2(0,T;H^{\tilde{r}_{k_p}}(\Gamma_{fp}))}\right) \\
&\quad + h^{r_{s_p}}\left(\|p_p\|_{L^\infty(0,T;H^{r_{s_p}}(\Omega_p))} + \|p_p\|_{L^2(0,T;H^{r_{s_p}}(\Omega_p))} + \|\partial_t p_p\|_{L^2(0,T;H^{r_{s_p}}(\Omega_p))}\right) \\
&\quad + h^{r_{k_s}}\Big(\|\boldsymbol{\eta}_p\|_{L^\infty(0,T;H^{r_{k_s}+1}(\Omega_p))} + \|\boldsymbol{\eta}_p\|_{L^2(0,T;H^{r_{k_s}+1}(\Omega_p))} + \|\partial_t \boldsymbol{\eta}_p\|_{L^2(0,T;H^{r_{k_s}+1}(\Omega_p))} \\
&\quad + \|\partial_t \boldsymbol{\eta}_p\|_{L^\infty(0,T;H^{r_{k_s}+1}(\Omega_p))} + \|\partial_{tt} \boldsymbol{\eta}_p\|_{L^2(0,T;H^{r_{k_s}+1}(\Omega_p))}\Big)\Big]. \\
&0 \le r_{k_f} \le k_f,\ 0 \le r_{s_f} \le s_f + 1,\ 1 \le \{r_{k_p}, \tilde{r}_{k_p}\} \le k_p + 1, \\
&0 \le r_{s_p} \le s_p + 1,\ 0 \le r_{k_s} \le k_s. \qquad (4.1)
\end{aligned}
$$

Proof We introduce the errors for all variables and split them into approximation and discretization errors:

$$
\begin{aligned}
\mathbf{e}_f &:= \mathbf{u}_f - \mathbf{u}_{f,h} = (\mathbf{u}_f - I_{f,h}\mathbf{u}_f) + (I_{f,h}\mathbf{u}_f - \mathbf{u}_{f,h}) := \boldsymbol{\chi}_f + \boldsymbol{\phi}_{f,h}, \\
\mathbf{e}_p &:= \mathbf{u}_p - \mathbf{u}_{p,h} = (\mathbf{u}_p - I_{p,h}\mathbf{u}_p) + (I_{p,h}\mathbf{u}_p - \mathbf{u}_{p,h}) := \boldsymbol{\chi}_p + \boldsymbol{\phi}_{p,h}, \\
\mathbf{e}_s &:= \boldsymbol{\eta}_p - \boldsymbol{\eta}_{p,h} = (\boldsymbol{\eta}_p - I_{s,h}\boldsymbol{\eta}_p) + (I_{s,h}\boldsymbol{\eta}_p - \boldsymbol{\eta}_{p,h}) := \boldsymbol{\chi}_s + \boldsymbol{\phi}_{s,h}, \\
e_{fp} &:= p_f - p_{f,h} = (p_f - Q_{f,h}p_f) + (Q_{f,h}p_f - p_{f,h}) := \chi_{fp} + \phi_{fp,h}, \\
e_{pp} &:= p_p - p_{p,h} = (p_p - Q_{p,h}p_p) + (Q_{p,h}p_p - p_{p,h}) := \chi_{pp} + \phi_{pp,h}, \\
e_\lambda &:= \lambda - \lambda_h = (\lambda - Q_{\lambda,h}\lambda) + (Q_{\lambda,h}\lambda - \lambda_h) := \chi_\lambda + \phi_{\lambda,h}, \qquad (4.2)
\end{aligned}
$$

where the operator $I = \left(I_{f,h}, I_{p,h}, I_{s,h}\right)$ satisfies, see Ambartsumyan et al. (2018b) for details,

$$
\begin{aligned}
b_\Gamma\left(I_{f,h}\mathbf{v}_f, I_{p,h}\mathbf{v}_p, I_{s,h}\boldsymbol{\xi}_p; \mu_h\right) &= 0, \qquad \forall \mu_h \in \Lambda_h, \qquad (4.3) \\
b_f(I_{f,h}\mathbf{v}_f - \mathbf{v}_f, w_{f,h}) &= 0, \qquad \forall w_{f,h} \in W_{f,h}, \qquad (4.4) \\
b_p(I_{p,h}\mathbf{v}_p - \mathbf{v}_p, w_{p,h}) &= 0, \qquad \forall w_{p,h} \in W_{p,h}, \qquad (4.5)
\end{aligned}
$$

and $Q_{f,h}$, $Q_{p,h}$ and $Q_{\lambda,h}$ are the L^2–projection operators such that

$$
\begin{aligned}
(p_f - Q_{f,h}p_f, w_{f,h})_{\Omega_f} &= 0, \qquad \forall\, w_{f,h} \in W_{f,h}, \qquad (4.6) \\
(p_p - Q_{p,h}p_p, w_{p,h})_{\Omega_p} &= 0, \qquad \forall\, w_{p,h} \in W_{p,h}, \qquad (4.7) \\
\langle \lambda - Q_{\lambda,h}\lambda, \mu_h\rangle_{\Gamma_{fp}} &= 0, \qquad \forall\, \mu_h \in \Lambda_h. \qquad (4.8)
\end{aligned}
$$

The operators have the following approximation properties:

$$
\|p_f - Q_{f,h}p_f\|_{L^2(\Omega_f)} \le Ch^{r_{s_f}}\|p_f\|_{H^{r_{s_f}}(\Omega_f)}, \qquad 0 \le r_{s_f} \le s_f + 1, \qquad (4.9)
$$

$$\|p_p - Q_{p,h}p_p\|_{L^2(\Omega_p)} \le Ch^{r_{s_p}}\|p_p\|_{H^{r_{s_p}}(\Omega_p)}, \qquad 0 \le r_{s_p} \le s_p + 1, \tag{4.10}$$

$$\|\lambda - Q_{\lambda,h}\lambda\|_{L^2(\Gamma_{fp})} \le Ch^{r_{k_p}}\|\lambda\|_{H^{r_{k_p}}(\Gamma_{fp})}, \qquad 0 \le \tilde{r}_{k_p} \le k_p + 1, \tag{4.11}$$

$$\|\mathbf{v}_f - I_{f,h}\mathbf{v}_f\|_{H^1(\Omega_f)} \le Ch^{r_{k_f}}\|\mathbf{v}_f\|_{H^{r_{k_f}+1}(\Omega_f)}, \qquad 0 \le r_{k_f} \le k_f, \tag{4.12}$$

$$\|\boldsymbol{\xi}_p - I_h^s\boldsymbol{\xi}_p\|_{H^m(\Omega_p)} \le Ch^{r_{k_s}-m}\|\boldsymbol{\xi}_p\|_{H^{r_{k_s}}(\Omega_p)}, \quad m = 0, 1, \quad 1 \le r_{k_s} \le k_s + 1, \tag{4.13}$$

$$\begin{aligned}&\|\mathbf{v}_p - I_{p,h}\mathbf{v}_p\|_{L^2(\Omega_p)}\\ &\quad\le C\left(h^{r_{k_p}}\|\mathbf{v}_p\|_{H^{r_{k_p}}(\Omega_p)} + h^{r_{k_f}}\|\mathbf{v}_f\|_{H^{r_{k_f}+1}(\Omega_f)} + h^{r_{k_s}}\|\boldsymbol{\xi}_p\|_{H^{r_{k_s}+1}(\Omega_p)}\right),\\ &\quad 1 \le r_{k_p} \le k_p + 1,\ 0 \le r_{k_f} \le k_f,\ 0 \le r_{k_s} \le k_s.\end{aligned} \tag{4.14}$$

To obtain a velocity bound in $L^\infty(0, T)$, we differentiate (2.11) and (3.2) in time, and then subtract (3.2)–(3.3) from (2.11)–(2.12) to form the error equation

$$\begin{aligned}&a_f(\partial_t\mathbf{e}_f, \mathbf{v}_{f,h}) + a_p^d(\partial_t\mathbf{e}_p, \mathbf{v}_{p,h}) + a_p^e(\partial_t\mathbf{e}_s, \boldsymbol{\xi}_{p,h}) + a_{BJS}(\partial_t\mathbf{e}_f, \partial_{tt}\mathbf{e}_s; \mathbf{v}_{f,h}, \boldsymbol{\xi}_{p,h})\\ &\quad + b_f(\mathbf{v}_{f,h}, \partial_t e_{fp}) + b_p(\mathbf{v}_{p,h}, \partial_t e_{pp}) + \alpha b_p(\boldsymbol{\xi}_{p,h}, \partial_t e_{pp})\\ &\quad + b_\Gamma(\mathbf{v}_{f,h}, \mathbf{v}_{p,h}, \boldsymbol{\xi}_{p,h}; \partial_t e_\lambda) + \left(s_0\,\partial_t e_{pp}, w_{p,h}\right)\\ &\quad - \alpha b_p(\partial_t e_s, w_{p,h}) - b_p(\mathbf{e}_p, w_{p,h}) - b_f(\mathbf{e}_f, w_{f,h}) = 0.\end{aligned}$$

Setting $\mathbf{v}_{f,h} = \boldsymbol{\phi}_{f,h}, \mathbf{v}_{p,h} = \boldsymbol{\phi}_{p,h}, \boldsymbol{\xi}_{p,h} = \partial_t\boldsymbol{\phi}_{s,h}, w_{f,h} = \partial_t\phi_{fp,h}$, and $w_{p,h} = \partial_t\phi_{pp,h}$, we have

$$\begin{aligned}&a_f(\partial_t\boldsymbol{\chi}_f, \boldsymbol{\phi}_{f,h}) + a_f(\partial_t\boldsymbol{\phi}_{f,h}, \boldsymbol{\phi}_{f,h}) + a_p^d(\partial_t\boldsymbol{\chi}_p, \boldsymbol{\phi}_{p,h})\\ &\quad + a_p^d(\partial_t\boldsymbol{\phi}_{p,h}, \boldsymbol{\phi}_{p,h}) + a_p^e\left(\partial_t\boldsymbol{\chi}_s, \partial_t\boldsymbol{\phi}_{s,h}\right)\\ &\quad + a_p^e\left(\partial_t\boldsymbol{\phi}_{s,h}, \partial_t\boldsymbol{\phi}_{s,h}\right) + a_{BJS}\left(\partial_t\boldsymbol{\chi}_f, \partial_{tt}\boldsymbol{\chi}_s; \boldsymbol{\phi}_{f,h}, \partial_t\boldsymbol{\phi}_{s,h}\right)\\ &\quad + a_{BJS}\left(\partial_t\boldsymbol{\phi}_{f,h}, \partial_{tt}\boldsymbol{\phi}_{s,h}; \boldsymbol{\phi}_{f,h}, \partial_t\boldsymbol{\phi}_{s,h}\right)\\ &\quad + b_f(\boldsymbol{\phi}_{f,h}, \partial_t\chi_{fp}) + b_f(\boldsymbol{\phi}_{f,h}, \partial_t\phi_{fp,h}) + b_p(\boldsymbol{\phi}_{p,h}, \partial_t\chi_{pp})\\ &\quad + b_p(\boldsymbol{\phi}_{p,h}, \partial_t\phi_{pp,h}) + \alpha b_p\left(\partial_t\boldsymbol{\phi}_{s,h}, \partial_t\chi_{pp}\right)\\ &\quad + \alpha b_p\left(\partial_t\boldsymbol{\phi}_{s,h}, \partial_t\phi_{pp,h}\right)\\ &\quad + b_\Gamma\left(\boldsymbol{\phi}_{f,h}, \boldsymbol{\phi}_{p,h}, \partial_t\boldsymbol{\phi}_{s,h}; \partial_t\chi_\lambda\right) + b_\Gamma\left(\boldsymbol{\phi}_{f,h}, \boldsymbol{\phi}_{p,h}, \partial_t\boldsymbol{\phi}_{s,h}; \partial_t\phi_{\lambda,h}\right)\\ &\quad + \left(s_0\,\partial_t\chi_{pp}, \partial_t\phi_{pp,h}\right) + \left(s_0\,\partial_t\phi_{pp,h}, \partial_t\phi_{pp,h}\right)\\ &\quad - \alpha b_p\left(\partial_t\boldsymbol{\chi}_s, \partial_t\phi_{pp,h}\right) - \alpha b_p\left(\partial_t\boldsymbol{\phi}_{s,h}, \partial_t\phi_{pp,h}\right)\\ &\quad - b_p(\boldsymbol{\chi}_p, \partial_t\phi_{pp,h}) - b_p(\boldsymbol{\phi}_{p,h}, \partial_t\phi_{pp,h})\\ &\quad - b_f(\boldsymbol{\chi}_f, \partial_t\phi_{fp,h}) - b_f(\boldsymbol{\phi}_{f,h}, \partial_t\phi_{fp,h}) = 0.\end{aligned} \tag{4.15}$$

The following terms simplify, due to the projection operators properties (4.7),(4.8), (4.4), and (4.5):

$$b_f(\boldsymbol{\chi}_f, \partial_t\phi_{fp,h}) = b_p(\boldsymbol{\chi}_p, \partial_t\phi_{pp,h}) = b_p(\boldsymbol{\phi}_{p,h}, \partial_t\chi_{pp}) = 0,$$

$$\left(s_0\,\partial_t\chi_{pp},\,\partial_t\phi_{pp,h}\right)=\langle\boldsymbol{\phi}_{p,h}\cdot\mathbf{n}_p,\,\partial_t\chi_\lambda\rangle_{\Gamma_{fp}}=0, \tag{4.16}$$

where we also used that $\Lambda_h=\mathbf{V}_{p,h}\cdot\mathbf{n}_p|_{\Gamma_{fp}}$ for the last equality. We also have

$$\begin{aligned}&b_\Gamma\left(\boldsymbol{\phi}_{f,h},\boldsymbol{\phi}_{p,h},\partial_t\boldsymbol{\phi}_{s,h};\partial_t\phi_{\lambda,h}\right)=0,\quad b_\Gamma\left(\boldsymbol{\phi}_{f,h},\boldsymbol{\phi}_{p,h},\partial_t\boldsymbol{\phi}_{s,h};\partial_t\chi_\lambda\right)\\&\quad=\left\langle\boldsymbol{\phi}_{f,h}\cdot\mathbf{n}_f+\partial_t\boldsymbol{\phi}_{s,h}\cdot\mathbf{n}_p,\,\partial_t\chi_\lambda\right\rangle_{\Gamma_{fp}},\end{aligned}$$

where we have used (4.3) and (3.4) for the first equality and the last equality in (4.16) for the second equality. Using these results, the error equation (4.15) becomes

$$\begin{aligned}&\frac{1}{2}\partial_t\left(a_f(\boldsymbol{\phi}_{f,h},\boldsymbol{\phi}_{f,h})+a_p^d(\boldsymbol{\phi}_{p,h},\boldsymbol{\phi}_{p,h})+\left|\boldsymbol{\phi}_{f,h}-\partial_t\boldsymbol{\phi}_{s,h}\right|_{a_{BJS}}^2\right)\\&\quad+a_p^e(\partial_t\boldsymbol{\phi}_{s,h},\partial_t\boldsymbol{\phi}_{s,h})+s_0\|\partial_t\phi_{pp,h}\|_{L^2(\Omega_p)}^2\\&=a_f(\partial_t\boldsymbol{\chi}_f,\boldsymbol{\phi}_{f,h})+a_p^d(\partial_t\boldsymbol{\chi}_p,\boldsymbol{\phi}_{p,h})+a_p^e\left(\partial_t\boldsymbol{\chi}_s,\partial_t\boldsymbol{\phi}_{s,h}\right)\\&\quad+\sum_{j=1}^{d-1}\left\langle\nu\alpha_{BJS}\sqrt{K_j^{-1}}\partial_t(\boldsymbol{\chi}_f-\partial_t\boldsymbol{\chi}_s)\cdot\boldsymbol{\tau}_{f,j},(\boldsymbol{\phi}_{f,h}-\partial_t\boldsymbol{\phi}_{s,h})\cdot\boldsymbol{\tau}_{f,j}\right\rangle_{\Gamma_{fp}}\\&\quad-b_f(\boldsymbol{\phi}_{f,h},\partial_t\chi_{fp})-\alpha b_p(\partial_t\boldsymbol{\phi}_{s,h},\partial_t\chi_{pp})+\alpha b_p(\partial_t\boldsymbol{\chi}_s,\partial_t\phi_{pp,h})\\&\quad-\langle\boldsymbol{\phi}_{f,h}\cdot\mathbf{n}_f+\partial_t\boldsymbol{\phi}_{s,h}\cdot\mathbf{n}_p,\partial_t\chi_\lambda\rangle_{\Gamma_{fp}}\\&\le C\left(\|\boldsymbol{\phi}_{f,h}\|_{H^1(\Omega_f)}^2+\|\boldsymbol{\phi}_{p,h}\|_{L^2(\Omega_p)}^2+\left|\boldsymbol{\phi}_{f,h}-\partial_t\boldsymbol{\phi}_{s,h}\right|_{a_{BJS}}^2\right)+\epsilon\|\partial_t\boldsymbol{\phi}_{s,h}\|_{H^1(\Omega_p)}^2\\&\quad+C\left(\|\partial_t\boldsymbol{\chi}_f\|_{H^1(\Omega_f)}^2+\|\partial_t\boldsymbol{\chi}_p\|_{L^2(\Omega_p)}^2+\|\partial_t\boldsymbol{\chi}_s\|_{H^1(\Omega_p)}^2+\|\partial_{tt}\boldsymbol{\chi}_s\|_{H^1(\Omega_p)}^2\right.\\&\quad\left.+\alpha b_p(\partial_t\boldsymbol{\chi}_s,\partial_t\phi_{pp,h})+\|\partial_t\chi_{fp}\|_{L^2(\Omega_f)}^2+\|\partial_t\chi_{pp}\|_{L^2(\Omega_p)}^2+\|\partial_t\chi_\lambda\|_{L^2(\Gamma_{fp})}^2\right),\end{aligned} \tag{4.17}$$

where we used the Cauchy–Schwartz, Young's and trace inequalities. Using the coercivity of the bilinear forms $a_f(\cdot,\cdot)$, $a_p^d(\cdot,\cdot)$, and $a_p^e(\cdot,\cdot)$, choosing ϵ small enough, and integrating (4.17) in time from 0 to an arbitrary $t\in(0,T]$ gives

$$\begin{aligned}&\|\boldsymbol{\phi}_{f,h}(t)\|_{H^1(\Omega_f)}^2+\|\boldsymbol{\phi}_{p,h}(t)\|_{L^2(\Omega_p)}^2+\left|\boldsymbol{\phi}_{f,h}(t)-\partial_t\boldsymbol{\phi}_{s,h}(t)\right|_{a_{BJS}}^2\\&\quad+\int_0^t\left(\|\partial_t\boldsymbol{\phi}_{s,h}\|_{H^1(\Omega_p)}^2+s_0\|\partial_t\phi_{pp,h}\|_{L^2(\Omega_p)}^2\right)ds\\&\le\|\boldsymbol{\phi}_{f,h}(0)\|_{H^1(\Omega_f)}^2+\|\boldsymbol{\phi}_{p,h}(0)\|_{L^2(\Omega_p)}^2+\left|\boldsymbol{\phi}_{f,h}(0)-\partial_t\boldsymbol{\phi}_{s,h}(0)\right|_{a_{BJS}}^2\\&\quad+C\int_0^t\left(\|\boldsymbol{\phi}_{f,h}\|_{H^1(\Omega_f)}^2+\|\boldsymbol{\phi}_{p,h}\|_{L^2(\Omega_p)}^2+\left|\boldsymbol{\phi}_{f,h}-\partial_t\boldsymbol{\phi}_{s,h}\right|_{a_{BJS}}^2\right.\\&\quad+\|\partial_t\boldsymbol{\chi}_f\|_{H^1(\Omega_f)}^2+\|\partial_t\boldsymbol{\chi}_p\|_{L^2(\Omega_p)}^2+\|\partial_t\boldsymbol{\chi}_s\|_{H^1(\Omega_p)}^2+\|\partial_{tt}\boldsymbol{\chi}_s\|_{H^1(\Omega_p)}^2\\&\quad\left.+\|\partial_t\chi_{fp}\|_{L^2(\Omega_f)}^2+\|\partial_t\chi_{pp}\|_{L^2(\Omega_p)}^2+\|\partial_t\chi_\lambda\|_{L^2(\Gamma_{fp})}^2+\alpha b_p(\partial_t\boldsymbol{\chi}_s,\partial_t\phi_{pp,h})\right)ds.\end{aligned} \tag{4.18}$$

Using integration by parts for the last term, we get

$$\begin{aligned}
&\int_0^t \alpha b_p(\partial_t \boldsymbol{\chi}_s, \partial_t \phi_{pp,h})\, ds = \alpha b_p(\partial_t \boldsymbol{\chi}_s(t), \phi_{pp,h}(t)) - \alpha b_p(\partial_t \boldsymbol{\chi}_s(0), \phi_{pp,h}(0)) \\
&\quad - \int_0^t \alpha b_p(\partial_{tt} \boldsymbol{\chi}_{s,h}, \phi_{pp,h})\, ds \\
&\quad \le \epsilon \left(\|\phi_{pp,h}(t)\|^2_{L^2(\Omega_p)} + \int_0^t \|\phi_{pp,h}\|^2_{L^2(\Omega_p)} \right) \\
&\quad + C \left(\|\partial_t \boldsymbol{\chi}_s(t)\|^2_{H^1(\Omega_p)} + \|\phi_{pp,h}(0)\|^2_{L^2(\Omega_p)} + \|\partial_t \boldsymbol{\chi}_s(0)\|^2_{H^1(\Omega_p)} \right. \\
&\quad \left. + \int_0^t \|\partial_{tt} \boldsymbol{\chi}_s\|^2_{H^1(\Omega_p)}\, ds \right).
\end{aligned} \tag{4.19}$$

Next, using an inf-sup condition for the Stokes–Darcy problem (Galvis and Sarkis 2007; Ambartsumyan et al. 2018b) and the error equation obtained by subtracting (3.2) from (2.11) and taking $\boldsymbol{\xi}_{p,h} = 0$, we obtain

$$\begin{aligned}
&\|(\phi_{fp,h}, \phi_{pp,h}, \phi_{\lambda,h})\|_{W_f \times W_p \times \Lambda_h} \\
&\quad \le C \sup_{0 \neq \mathbf{v}_h \in \mathbf{V}_h} \frac{b_f(\mathbf{v}_{f,h}, \phi_{fp,h}) + b_p(\mathbf{v}_{p,h}, \phi_{pp,h}) + b_\Gamma(\mathbf{v}_{f,h}, \mathbf{v}_{p,h}, 0; \phi_{\lambda,h})}{\|\mathbf{v}_h\|_{\mathbf{V}}} \\
&\quad = C \sup_{0 \neq \mathbf{v}_h \in \mathbf{V}_h} \left(\frac{-a_f(\mathbf{e}_f, \mathbf{v}_{f,h}) - a_p^d(\mathbf{e}_p, \mathbf{v}_{p,h}) - a_{BJS}(\mathbf{e}_f, \partial_t \mathbf{e}_s; \mathbf{v}_{f,h}, 0)}{\|\mathbf{v}_h\|_{\mathbf{V}}} \right. \\
&\qquad \left. + \frac{-b_f(\mathbf{v}_{f,h}, \chi_{fp}) - b_p(\mathbf{v}_{p,h}, \chi_{pp}) - b_\Gamma(\mathbf{v}_{f,h}, \mathbf{v}_{p,h}, 0; \chi_\lambda)}{\|\mathbf{v}_h\|_{\mathbf{V}}} \right).
\end{aligned}$$

We have $b_p(\mathbf{v}_{p,h}, \chi_{pp}) = 0$ and $\langle \mathbf{v}_{p,h} \cdot \mathbf{n}_p, \chi_\lambda \rangle_{\Gamma_{fp}} = 0$. Then, using the continuity of the bilinear forms and the trace inequality, we get

$$\begin{aligned}
&\epsilon(\|\phi_{fp,h}\|^2_{L^2(\Omega_f)} + \|\phi_{pp,h}\|^2_{L^2(\Omega_p)} + \|\phi_{\lambda,h}\|^2_{L^2(\Gamma_{fp})}) \\
&\quad \le C\epsilon \left(\|\boldsymbol{\phi}_{f,h}\|^2_{H^1(\Omega_f)} + \|\boldsymbol{\phi}_{p,h}\|^2_{L^2(\Omega_p)} + \|\boldsymbol{\phi}_{s,h}\|^2_{H^1(\Omega_p)} + |\boldsymbol{\phi}_{f,h} - \partial_t \boldsymbol{\phi}_{s,h}|^2_{a_{BJS}} \right. \\
&\qquad + \|\boldsymbol{\chi}_f\|^2_{H^1(\Omega_f)} + \|\boldsymbol{\chi}_p\|^2_{L^2(\Omega_p)} + \|\boldsymbol{\chi}_s\|^2_{H^1(\Omega_p)} + \|\partial_t \boldsymbol{\chi}_s\|^2_{H^1(\Omega_p)} \\
&\qquad \left. + \|\chi_{fp}\|^2_{L^2(\Omega_f)} + \|\chi_{pp}\|^2_{L^2(\Omega_p)} + \|\chi_\lambda\|_{L^2(\Gamma_{fp})} \right).
\end{aligned} \tag{4.20}$$

Finally, to control the error at $t = 0$, we note that the assumed solution regularity on the right hand side of (4.1) implies that (2.11)–(2.13) and (3.2)–(3.4) hold at $t = 0$. We subtract (3.2)–(3.3) from (2.11)–(2.12) at $t = 0$, sum the two equations, and take $\mathbf{v}_{f,h} = \boldsymbol{\phi}_{f,h}$, $\mathbf{v}_{p,h} = \boldsymbol{\phi}_{p,h}$, $\boldsymbol{\xi}_{p,h} = \partial_t \boldsymbol{\phi}_{s,h}$, $w_{f,h} = \phi_{fp,h}$, and $w_{p,h} = \phi_{pp,h}$, to obtain

$$\begin{aligned}
&a_f(\boldsymbol{\phi}_{f,h}(0), \boldsymbol{\phi}_{f,h}(0)) + a_p^d(\boldsymbol{\phi}_{p,h}(0), \boldsymbol{\phi}_{p,h}(0)) + |\boldsymbol{\phi}_{f,h}(0) - \partial_t \boldsymbol{\phi}_{s,h}(0)|^2_{a_{BJS}} \\
&\quad = -a_p^e(\boldsymbol{\phi}_{s,h}(0), \partial_t \boldsymbol{\phi}_{s,h}(0)) - s_0(\partial_t \phi_{pp,h}(0), \phi_{pp,h}(0))_{\Omega_p}
\end{aligned}$$

$$
\begin{aligned}
&+ a_f(\boldsymbol{\chi}_f(0), \boldsymbol{\phi}_{f,h}(0)) + a_p^d(\boldsymbol{\chi}_p(0), \boldsymbol{\phi}_{p,h}(0)) + a_p^e\left(\boldsymbol{\chi}_s(0), \partial_t \boldsymbol{\phi}_{s,h}(0)\right) \\
&+ \sum_{j=1}^{d-1} \left\langle \mu \alpha_{BJS} \sqrt{K_j^{-1}} (\boldsymbol{\chi}_f(0) - \partial_t \boldsymbol{\chi}_s(0)) \cdot \boldsymbol{\tau}_{f,j}, (\boldsymbol{\phi}_{f,h}(0) - \partial_t \boldsymbol{\phi}_{s,h}(0)) \cdot \boldsymbol{\tau}_{f,j} \right\rangle_{\Gamma_{fp}} \\
&- b_f(\boldsymbol{\phi}_{f,h}(0), \chi_{fp}(0)) + \alpha b_p(\partial_t \boldsymbol{\phi}_{s,h}(0), \chi_{pp}(0)) + \alpha b_p(\partial_t \boldsymbol{\chi}_s(0), \phi_{pp,h}(0)) \\
&+ \langle \boldsymbol{\phi}_{f,h}(0) \cdot \mathbf{n}_f + \partial_t \boldsymbol{\phi}_{s,h}(0) \cdot \mathbf{n}_p, \chi_\lambda(0) \rangle_{\Gamma_{fp}}.
\end{aligned}
$$

Since $p_{p,h}(0) = Q_{p,h} p_{p,0}$ and $\boldsymbol{\eta}_{p,h}(0) = I_{s,h} \boldsymbol{\eta}_{p,0}$, we have that $\phi_{pp,h}(0) = 0$ and $\boldsymbol{\phi}_{s,h}(0) = 0$. Since $p_{p,0}$ and $\boldsymbol{\eta}_{p,0}$ are constants, we also have that $\boldsymbol{\chi}_s = 0$, $\chi_{pp} = 0$, and $\chi_\lambda = 0$. It is then easy to see that

$$
\begin{aligned}
&\|\boldsymbol{\phi}_{f,h}(0)\|^2_{H^1(\Omega_f)} + \|\boldsymbol{\phi}_{p,h}(0)\|^2_{L^2(\Omega_p)} + \left|\boldsymbol{\phi}_{f,h}(0) - \partial_t \boldsymbol{\phi}_{s,h}(0)\right|^2_{a_{BJS}} \\
&\quad \le C(\|\boldsymbol{\chi}_f\|^2_{H^1(\Omega_f)} + \|\boldsymbol{\chi}_p\|^2_{L^2(\Omega_p)} + \|\chi_{fp}\|^2_{L^2(\Omega_f)}).
\end{aligned} \tag{4.21}
$$

The assertion of the lemma follows from combining (4.18)–(4.21) and using Gronwall's inequality, the triangle inequality, and the approximation properties (4.9)–(4.14). □

Lemma 4.2 *Under the assumptions of Lemma 4.1, for any choice of stable spaces when $d = 2$, and for $k_f \ge 2$, $k_p \ge 1$, $s_p \ge 1$, and $k_s \ge 2$ when $d = 3$, there exists a positive constant $M = M(\mathbf{u}_f, p_f, \mathbf{u}_p, p_p, \boldsymbol{\eta}_p, \lambda)$, such that, for $t \in (0, T]$, the solution $\mathbf{u}_h$ of (3.2)–(3.4) satisfies*

$$
\|\mathbf{u}_h\|_{L^\infty(\Omega)} \le M. \tag{4.22}
$$

Proof We recall that by definition

$$
\mathbf{u}_h = \begin{cases} \mathbf{u}_{f,h} & \text{in } \Omega_f, \\ \mathbf{u}_{p,h} & \text{in } \Omega_p. \end{cases}
$$

Therefore, we prove (4.22) separately for $\mathbf{u}_{f,h}$ in the fluid domain and for $\mathbf{u}_{p,h}$ in the poroelastic domain. Let $S_{f,h}$ be the Scott-Zhang interpolant onto $\mathbf{V}_{f,h}$ (Scott and Zhang 1990), satisfying

$$
\|S_{f,h}\mathbf{v}_f\|_{\infty,\Omega_f} \le C(\|\mathbf{v}_f\|_{\infty,\Omega_f} + h\|\nabla \mathbf{v}_f\|_{\infty,\Omega_f}), \qquad \forall \mathbf{v}_f \in W^{1,\infty}(\Omega_f), \tag{4.23}
$$

$$
\|\mathbf{v}_f - S_{f,h}\mathbf{v}_f\|_{\Omega_f} \le C h^{r_{k_f}} \|\mathbf{v}_f\|_{r_{k_f},\Omega_f}, \quad 1 \le r_{k_f} \le k_f + 1, \quad \forall \mathbf{v}_f \in H^{r_{k_f}}(\Omega_f). \tag{4.24}
$$

By the triangle inequality,

$$
\|\mathbf{u}_{f,h}\|_{L^\infty(\Omega_f)} \le \|\mathbf{u}_{f,h} - S_{f,h}\mathbf{u}_f\|_{L^\infty(\Omega_f)} + \|S_{f,h}\mathbf{u}_f\|_{L^\infty(\Omega_f)}. \tag{4.25}
$$

To obtain a bound on $\|\mathbf{u}_{f,h} - S_{f,h}\mathbf{u}_f\|_{L^\infty(\Omega_f)}$, we use a scaling argument via mapping to the reference element $\hat{E}$. Recall that, due to shape regularity, the determinant of the Jacobian matrix satisfies $\|J_E\|_{\infty,\hat{E}} \sim h^d$. Therefore, for any $E \in \mathcal{T}_h^f \cup \mathcal{T}_h^p$ and any polynomial $\mathbf{v}_h$ on E, using norm equivalence on $\hat{E}$, we have

$$\|\mathbf{v}_h\|_{\infty,E} \le \|\hat{\mathbf{v}}_h\|_{\infty,\hat{E}} \le \|\hat{\mathbf{v}}_h\|_{\hat{E}} \le Ch^{-d/2}\|\mathbf{v}_h\|_E.$$

Using the above bound, we have

$$\begin{aligned}\|\mathbf{u}_{f,h} - S_{f,h}\mathbf{u}_f\|_{L^\infty(\Omega_f)} &\le Ch^{-d/2}\|\mathbf{u}_{f,h} - S_{f,h}\mathbf{u}_f\|_{L^2(\Omega_f)} \\ &\le Ch^{-d/2}(\|\mathbf{u}_f - \mathbf{u}_{f,h}\|_{L^2(\Omega_f)} + \|\mathbf{u}_f - S_{f,h}\mathbf{u}_f\|_{L^2(\Omega_f)}),\end{aligned}$$

which, combined with (4.25), implies

$$\begin{aligned}\|\mathbf{u}_{f,h}\|_{L^\infty(\Omega_f)} \le Ch^{-d/2}&(\|\mathbf{u}_f - \mathbf{u}_{f,h}\|_{L^2(\Omega_f)} + \|\mathbf{u}_f - S_{f,h}\mathbf{u}_f\|_{L^2(\Omega_f)}) \\ &+\|S_{f,h}\mathbf{u}_f\|_{L^\infty(\Omega_f)}.\end{aligned} \tag{4.26}$$

Next, we consider the MFE interpolant $\Pi_{p,h}$ onto $\mathbf{V}_{p,h}$ that satisfies (Acosta et al. 2011)

$$\|\Pi_{p,h}\mathbf{v}_p\|_{\infty,\Omega_p} \le C\left(\|\mathbf{v}_p\|_{\infty,\Omega_p} + h\|\nabla\mathbf{v}_p\|_{\infty,\Omega_p}\right), \qquad \forall \mathbf{v}_p \in W^{1,\infty}(\Omega_p), \tag{4.27}$$

$$\|\mathbf{v}_p - \Pi_{p,h}\mathbf{v}_p\|_{\Omega_p} \le Ch^{r_{k_p}}\|\mathbf{v}_p\|_{r_{k_p},\Omega_p}, \quad 1 \le r_{k_p} \le k_p + 1, \quad \forall \mathbf{v}_p \in H^{r_{k_p}}(\Omega_p). \tag{4.28}$$

Similarly to (4.26) we obtain

$$\begin{aligned}\|\mathbf{u}_{p,h}\|_{L^\infty(\Omega_p)} \le Ch^{-d/2}&(\|\mathbf{u}_p - \mathbf{u}_{p,h}\|_{L^2(\Omega_p)} + \|\mathbf{u}_p - \Pi_{p,h}\mathbf{u}_p\|_{L^2(\Omega_f)}) \\ &+\|\Pi_{p,h}\mathbf{u}_p\|_{L^\infty(\Omega_p)}.\end{aligned} \tag{4.29}$$

The proof is completed by combining (4.26), (4.29), (4.23)–(4.24), (4.27)–(4.28), and (4.1). □

Remark 4.1 We note that the above result assumes sufficient regularity of the solution, as indicated by (4.23)–(4.24), (4.27)–(4.28), and (4.1).

We will utilize the following positive definite property of the dispersion tensor, proved in Sun et al. (2002).

Lemma 4.3 *Assume that for* $\mathbf{D}(\mathbf{u})$ *defined in* (2.15), $d_m(\mathbf{x}) \ge d_{m,*} > 0, \alpha_l(\mathbf{x}) \ge 0$ *and* $\alpha_t(\mathbf{x}) \ge 0$ *uniformly in* Ω. *Then* $\mathbf{D}(\mathbf{u})$ *is uniformly positive definite and for all* $\mathbf{x} \in \Omega$,

$$\mathbf{D}(\mathbf{u})\nabla c \cdot \nabla c \ge d_{m,*}|\nabla c|^2. \tag{4.30}$$

We next prove a Gårding's inequality for the bilinear form $B_{\mathbf{u}_h}(\cdot,\cdot)$. To simplify the analysis we assume velocity boundary condition for the Darcy problem.

Lemma 4.4 *Under the assumptions of Lemma 4.2, and if* $\Gamma_p^D = \emptyset$*, then the bilinear form* $B_{\mathbf{u}_h}(\cdot,\cdot)$ *defined in (3.6) satisfies,* $\forall t \in (0,T]$*,*

$$B_{\mathbf{u}_h}(\psi_h,\psi_h) \geq C\left(|||\nabla\psi_h|||_\Omega^2 + J^\sigma(\psi_h,\psi_h) - \|\psi_h\|_\Omega^2\right), \quad \forall \psi_h \in \mathcal{D}_f(\mathcal{T}_h). \tag{4.31}$$

Proof For any $\psi_h \in \mathcal{D}_f(\mathcal{T}_h)$ we have

$$\begin{aligned} B_{\mathbf{u}_h}(\psi_h,\psi_h) = &\sum_{E\in\mathcal{T}_h}\int_E (\mathbf{D}(\mathbf{u}_h)\nabla\psi_h - \psi_h\mathbf{u}_h)\cdot\nabla\psi_h - \sum_{e\in E_h}\int_e \{\mathbf{D}(\mathbf{u}_h)\nabla\psi_h\cdot\mathbf{n}_e\}[\psi_h] \\ &+ \sum_{e\in E_h}\int_e \{\mathbf{D}(\mathbf{u}_h)\nabla\psi_h\cdot\mathbf{n}_e\}[\psi_h] + \sum_{e\in E_h}\int_e \psi_h^*\mathbf{u}_h\cdot\mathbf{n}_e[\psi_h] \\ &+ \int_{\Gamma_{out}} \psi_h\mathbf{u}_h\cdot\mathbf{n}\,\psi_h - \int_\Omega \psi_h q^-\psi_h + J_0^\sigma(\psi_h,\psi_h). \end{aligned} \tag{4.32}$$

Next we introduce the notation

$$J_1 := \sum_{E\in\mathcal{T}_h}\int_E (\mathbf{D}(\mathbf{u}_h)\nabla\psi_h - \psi_h\mathbf{u}_h)\cdot\nabla\psi_h, \quad J_2 := \sum_{e\in E_h}\int_e \psi_h^*[\psi_h]\mathbf{u}_h\cdot\mathbf{n}_e,$$
$$J_3 := \int_{\Gamma_{out}} \psi_h^2\,\mathbf{u}_h\cdot\mathbf{n} - \int_\Omega q^-\psi_h^2 + J_0^\sigma(\psi_h,\psi_h),$$

and rewrite (4.32) as

$$B_{\mathbf{u}_h}(\psi_h,\psi_h) = J_1 + J_2 + J_3. \tag{4.33}$$

Using (4.22) and (4.30), we bound J_1 as

$$\begin{aligned} J_1 = &\sum_{E\in\mathcal{T}_h}\int_E \mathbf{D}(\mathbf{u}_h)\nabla\psi_h\cdot\nabla\psi_h - \sum_{E\in\mathcal{T}_h}\int_E \psi_h\mathbf{u}_h\cdot\nabla\psi_h \geq d_{m,*}|||\nabla\psi_h|||_\Omega^2 \\ &- M\sum_{E\in\mathcal{T}_h}\|\psi_h\|_E\|\nabla\psi_h\|_E \\ \geq\ & d_{m,*}|||\nabla\psi_h|||_\Omega^2 - C\epsilon^{-1}\|\psi_h\|_\Omega^2 - \epsilon|||\nabla\psi_h|||_\Omega^2. \end{aligned} \tag{4.34}$$

For J_2 we have

$$\begin{aligned} J_2 = &\sum_{e\in E_h}\int_e \psi_h^*[\psi_h]\mathbf{u}_h\cdot\mathbf{n}_e \geq -M\left|\sum_{e\in E_h}\int_e \psi_h^*[\psi_h]\right| \geq -M\sum_{e\in E_h}\|\psi_h^*\|_e\|[\psi_h]\|_e \\ \geq & -\sum_{e\in E_h}\left(\frac{\epsilon\sigma_e}{h_e}\|[\psi_h]\|_e^2 + \frac{Ch_e}{\epsilon}\|\psi_h^*\|_e^2\right) \geq -\epsilon J^\sigma(\psi_h,\psi_h) - \frac{Ch}{\epsilon}\sum_{E\in\mathcal{T}_h} h^{-1}\|\psi_h\|_E^2 \\ \geq & -\epsilon J^\sigma(\psi_h,\psi_h) - C\epsilon^{-1}\|\psi_h\|_\Omega^2. \end{aligned} \tag{4.35}$$

We bound J_3, using that $\mathbf{u}_h \cdot \mathbf{n} = \mathbf{u} \cdot \mathbf{n} \geq 0$ on Γ_{out} and that $q^- \leq 0$,

$$J_3 = \int_{\Gamma_{out}} \psi_h^2 \mathbf{u} \cdot \mathbf{n} - \int_\Omega q^- \psi_h^2 + J_0^\sigma(\psi_h, \psi_h) \geq J_0^\sigma(\psi_h, \psi_h). \tag{4.36}$$

Combining (4.33)–(4.36) we obtain

$$B_{\mathbf{u}_h}(\psi_h, \psi_h) \geq (d_{m,*} - \epsilon) |||\nabla \psi_h|||_\Omega^2 - C\epsilon^{-1} \|\psi_h\|_\Omega^2 + (1-\epsilon) J^\sigma(\psi_h, \psi_h).$$

Choosing ϵ small enough completes the proof. □

We are now ready to prove a stability bound for the solution of (3.9).

Theorem 4.1 *Under the assumptions of Lemma 4.4, there exists a positive constant C independent of h such that the solution $c_h(t)$ of (3.9) satisfies, $\forall t \in (0, T]$,*

$$\|c_h(t)\|_\Omega^2 + \int_0^t |||\nabla c_h(s)|||_\Omega^2 \, ds \leq C \left(\|c_h(0)\|_\Omega^2 + \int_0^t \left(\|c_w(s) q^+(s)\|_\Omega^2 + \|c_{in}(s)\|_{\Gamma_{in}}^2 \right) ds \right).$$

Proof With the choice $\psi_h = c_h$, (3.9) reads

$$\int_\Omega \phi c_h \partial_t c_h + B_{\mathbf{u}_h}(c_h, c_h) = L_h(c_h).$$

Using (4.31), the definition (3.6) of L_h, and that $\mathbf{u}_h \cdot \mathbf{n} = \mathbf{u} \cdot \mathbf{n}$, we obtain

$$\begin{aligned} &\phi \frac{1}{2} \partial_t \|c_h\|_\Omega^2 + C \left(|||\nabla c_h|||_\Omega^2 + J^\sigma(c_h, c_h) \right) \\ &\quad \leq C \|c_h\|_\Omega^2 + \int_\Omega c_w q^+ c_h - \int_{\Gamma_{in}} c_{in} \mathbf{u} \cdot \mathbf{n} \, c_h. \end{aligned}$$

Integrating in time from $s = 0$ to $s = t$ for $0 < t \leq T$ and using Cauchy–Schwarz and Young's inequalities, we obtain

$$\begin{aligned} &\|c_h(t)\|_\Omega^2 + \int_0^t \left(|||\nabla c_h(s)|||_\Omega^2 + J^\sigma(c_h, c_h) \right) ds \\ &\leq C \left(\|c_h(0)\|_\Omega^2 + \int_0^t \left(\|c_h(s)\|_\Omega^2 + \|c_w(s) q^+(s)\|_\Omega^2 \right. \right. \\ &\quad \left. \left. + \epsilon^{-1} \|c_{in}(s)\|_{\Gamma_{in}}^2 + \epsilon \|c_h(s)\|_{\Gamma_{in}}^2 \right) ds \right). \end{aligned} \tag{4.37}$$

The last term above is bounded as

$$\|c_h\|_{\Gamma_{in}}^2 \leq C \left(\|c_h\|_\Omega^2 + |||\nabla c_h|||_\Omega^2 + J^\sigma(c_h, c_h) \right), \tag{4.38}$$

which can be shown following the argument presented in Brenner (2003). The theorem follows from (4.37)–(4.38), taking ϵ small enough, and using Gronwall's inequality. □

In the next theorem we state the error estimate for the transport problem (3.9). Derivation of the bound follows the steps in the proof of Theorem 4.1 in Sun et al. (2002), using the estimate (4.22), rather than a boundedness property of the "cut-off" operator. For the sake of space, we omit the proof and the reader is referred to Sun et al. (2002) for the details.

Theorem 4.2 *Under the assumptions of Lemma 4.4, and assuming further that the solution of (2.14)–(2.18) satisfies* $c \in L^\infty(0,T;W^{1,\infty}(\Omega)) \cap L^2(0,T;H^{r+1}(\Omega))$, *there exists a positive constant* C *independent of* h *such that,* $\forall t \in (0,T]$,

$$\|c(t)-c_h(t)\|_\Omega + \left(\int_0^t |||\nabla(c(s)-c_h(s))|||_\Omega^2\, ds\right)^{1/2} \leq Ch^{\min\{k_f,s_f+1,k_p+1,s_p+1,k_s,r\}}.$$

5 Numerical results

In this section, we present results from several computational experiments in two dimensions. The computations are performed using a fully discrete scheme with Backward Euler time discretization. The method is implemented using the finite element package FreeFem++ (Hecht 2012). We use a monolithic solver for the Stokes–Biot system at each time step. It is possible to design a non-overlapping domain decomposition algorithm, similar to the Stokes–Darcy problem, see e.g. Vassilev et al. (2014). One can also use various splitting schemes for the Biot system (Mikelić and Wheeler 2013; Kim et al. 2011b, a). We first present a numerical test that confirms the theoretical convergence rates for the Biot-Stokes-transport problem using an analytical solution, followed by five examples with simulations of fluid flow in a fractured reservoir with physically realistic parameters.

5.1 Convergence test

In this test we study the convergence of the spatial discretization using an analytical solution. The domain is a rectangle $\Omega = [0,1]\times[-1,1]$. We associate the upper half with the Stokes flow, while the lower half represents the flow in the poroelastic structure governed by the Biot system. The appropriate interface conditions are enforced along the interface $y = 0$. Following the example from Ambartsumyan et al. (2018b), the solution in the Stokes region is

$$\mathbf{u}_f = \pi\cos(\pi t)\begin{pmatrix}-3x+\cos(y)\\ y+1\end{pmatrix}, \quad p_f = e^t\sin(\pi x)\cos\left(\frac{\pi y}{2}\right)+2\pi\cos(\pi t).$$

Table 1 Relative numerical errors and convergence rates

$\mathcal{P}_1^b - \mathcal{P}_1$, $\mathcal{RT}_0 - \mathcal{P}_0$, $\mathcal{P}_1$, $\mathcal{P}_0$ and $\mathcal{P}_1^{dc}$								
	$\|\mathbf{u}_f - \mathbf{u}_{f,h}\|_{l^2(H^1(\Omega_f))}$		$\|\mathbf{u}_p - \mathbf{u}_{p,h}\|_{l^2(L^2(\Omega_p))}$		$\|\|\|c - c_h\|\|\|_{l^2(H^1(\Omega))}$		$\|c - c_h\|_{l^\infty(L^2(\Omega))}$	
h	Error	Rate	Error	Rate	Error	Rate	Error	Rate
1/4	1.79E-02	–	2.10E−01	–	2.24E−01	–	2.52E−02	–
1/8	8.96E−03	1.0	1.05E−01	1.0	1.14E−01	1.0	6.17E−03	2.0
1/16	4.47E−03	1.0	5.23E−02	1.0	5.71E−02	1.0	1.56E−03	2.0
1/32	2.24E−03	1.0	2.61E−02	1.0	2.87E−02	1.0	3.96E−04	2.0
1/64	1.12E−03	1.0	1.31E−02	1.0	1.44E−02	1.0	1.00E−04	2.0

The Biot solution is chosen accordingly to satisfy the interface conditions (2.5)–(2.7):

$$\mathbf{u}_p = \pi e^t \begin{pmatrix} \cos(\pi x)\cos(\frac{\pi y}{2}) \\ \frac{1}{2}\sin(\pi x)\sin(\frac{\pi y}{2}) \end{pmatrix}, \quad p_p = e^t \sin(\pi x)\cos\left(\frac{\pi y}{2}\right),$$
$$\boldsymbol{\eta}_p = \sin(\pi t)\begin{pmatrix} -3x + \cos(y) \\ y + 1 \end{pmatrix}.$$

The right hand side functions $\mathbf{f}_f$, q_f, $\mathbf{f}_p$ and q_p are computed from (2.1)–(2.4) using the above solution. The model problem is then complemented with the appropriate Dirichlet boundary conditions and initial data. The total simulation time for this test case is $T = 10^{-3}$ and the time step is $\Delta t = 10^{-4}$. The time step is chosen sufficiently small, so that the time discretization error does not affect the convergence rates. The transport solution is set to

$$c = t\left(\cos(\pi x) + \cos(\pi y)\right)/\pi,$$

with the diffusion tensor $\mathbf{D} = 10^{-3}\mathbf{I}$ and porosity $\phi = 1$.

For the spatial discretization we use the MINI elements $\mathcal{P}_1^b - \mathcal{P}_1$ for Stokes, the Raviart-Thomas $\mathcal{RT}_0 - \mathcal{P}_0$ for Darcy, continuous Lagrangian $\mathcal{P}_1$ elements for the displacement, and piecewise constant Lagrange multiplier $\mathcal{P}_0$. The transport equation is discretized using discontinuous piecewise linears, $\mathcal{P}_1^{dc}$. For simplicity the Stokes and Biot meshes are made matching along the interface and the transport mesh is the same as the flow mesh. Theorem 4.2 predicts first order convergence for all variables, which is confirmed by the results reported in Table 1. We also observe second order convergence for the concentration in the $l^\infty(L^2(\Omega))$ norm. Here the notation $l^2(\cdot)$ and $l^\infty(\cdot)$ refers to discrete-in-time norms.

5.2 Applications to coupled flow and transport through fractured poroelastic media

We present five examples with simulations of fluid flow in a fractured reservoir with physically realistic parameters. The examples are designed to illustrate the robustness

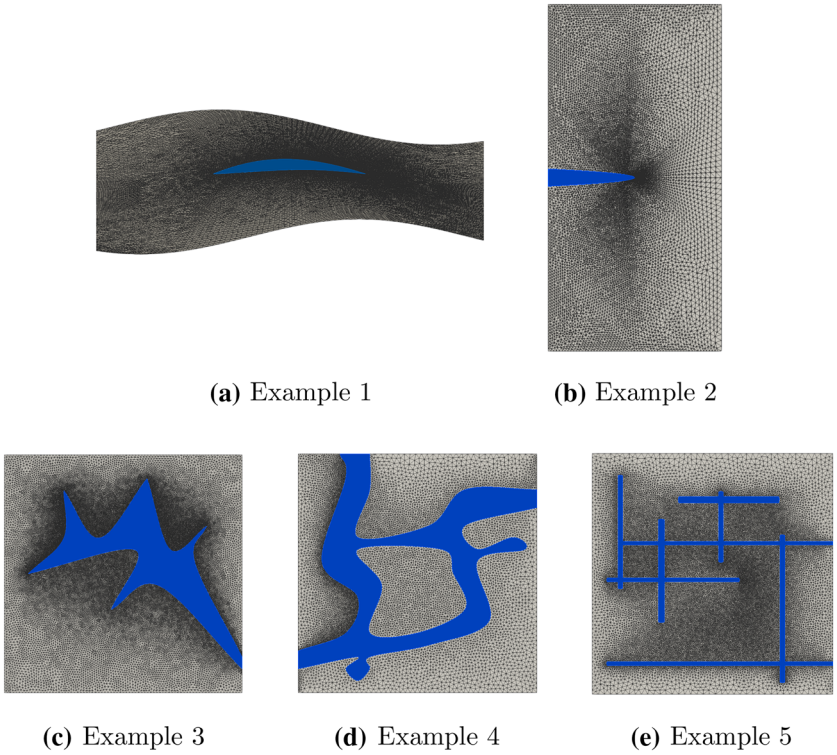

(a) Example 1 **(b)** Example 2

(c) Example 3 **(d)** Example 4 **(e)** Example 5

Fig. 2 Computational domains

of the method with respect to reservoir and fracture geometry, rock heterogeneities, and various flow and transport scenarios. The computational domains for the five examples are shown in Fig. 2. Examples 1 and 2 are motivated by hydraulic fracturing. Example 1 features irregularly shaped fracture and reservoir, with fluid injected in the center of the fracture. Example 2 has heterogeneous permeability, porosity, and Young's modulus, with fluid injected into the fracture via inflow boundary condition. Examples 3-5 model flow and transport through vuggy or naturally fractured poroelastic media. The flow is induced by a pressure drop between the left and right boundaries. The transport equation models the concentration of a tracer, which enters the domain with the fluid along the inflow boundary. The reservoir in Example 3 has a large irregularly shaped cavity. Examples 4 and 5 consider a network of channels and fractures, respectively. The latter is the computationally most challenging example, due to the small fracture thickness and sharp angles at the fracture intersections. For all examples in this section the physical units are meters for length, seconds for time, and kPa for pressure.

5.2.1 Example 1: fluid and tracer injection into a fracture

For this example, we first introduce the reference domain $\hat{\Omega}$ given by a square $[-1, 1]\times[-1, 1]$. A fracture, representing the reference fluid domain $\hat{\Omega}_f$, is then described by

Table 2 Poroelasticity and fluid parameters in Example 1

Parameter	Symbol	Units	Values
Young's modulus	E	(kPa)	10^7
Poisson's ratio	ν		0.2
Lamé coefficient	λ_p	(kPa)	$5/18 \times 10^7$
Lamé coefficient	μ_p	(kPa)	$5/12 \times 10^7$
Dynamic viscosity	μ	(kPa s)	10^{-6}
Permeability	K	(m^2)	$diag(200, 50) \times 10^{-12}$
Mass storativity	s_0	(kPa^{-1})	6.89×10^{-2}
Biot–Willis constant	α		1.0
Beavers–Joseph–Saffman coefficient	α_{BJS}		1.0

its top and bottom boundaries, as follows

$$\hat{y}^2 = 8^2(\hat{x} - 0.35)^2(\hat{x} + 0.35)^2, \quad \hat{x} \in [-0.35, 0.35].$$

The physical domain, see Fig. 2a, is obtained from the reference one $\hat{\Omega}$ via the mapping

$$\begin{bmatrix} x \\ y \end{bmatrix} = \begin{bmatrix} \hat{x} \\ 8\left(\cos\left(\frac{\pi\hat{x}+\hat{y}}{100}\right) + \frac{\hat{y}}{4}\right) \end{bmatrix}.$$

This example models the interaction between a fracture filled with fluid and a surrounding poroelastic reservoir. The physical parameters are given in the Table 2. They are taken from Girault et al. (2015) and are realistic for hydraulic fracturing.

The Lamé coefficients are determined from the Young's modulus E and the Poisson's ratio ν via the well-known relationships

$$\lambda_p = \frac{E\nu}{(1+\nu)(1-2\nu)}, \quad \mu_p = \frac{E}{2(1+\nu)}.$$

The boundary conditions are

$$p_p = 1000, \quad \boldsymbol{\eta}_p = 0 \text{ on } \Gamma_p.$$

The initial conditions are set accordingly to $\boldsymbol{\eta}_p(0) = 0$ and $p_p(0) = 1000$. The initial concentration is $c(0) = 0$. The total simulation time is $T = 100$ s with a time step of size $\Delta t = 1$s.

The flow is driven by the injection of the fluid into the fracture with the constant rate $5 \cdot 10^{-3}$ kg/s. The fluid is injected into a region obtained from mapping a disk of radius 0.017m at the center of the reference fracture $\hat{\Omega}_f$. A tracer is injected in this same region, continuously over the entire simulation period, i.e. $c_w = 1$ in the region specified above.

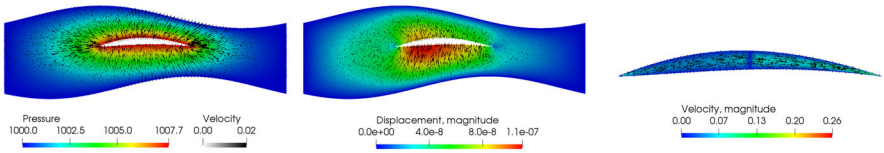

(a) Darcy velocity (m/s) over pressure (kPa) **(b)** Displacement (m) **(c)** Stokes velocity (m/s)

Fig. 3 Example 1, computed Stokes–Biot solution at $t = 100\,\mathrm{s}$

Recall, see (2.15), that the diffusion tensor is given as

$$\mathbf{D}(\mathbf{u}) = d_m\mathbf{I} + |\mathbf{u}|\{\alpha_l\mathbf{E} + \alpha_t(\mathbf{I} - \mathbf{E})\}.$$

For all examples in this section, in Ω_f we set $d_m = 10^{-6}$ m/s, $\alpha_l = \alpha_t = 0$, i.e., $\mathbf{D} = 10^{-6}\mathbf{I}$ m/s. In Ω_p we set $d_m = 10^{-4}$ m/s, $\alpha_l = \alpha_t = 10^{-4}$. The porosity is set to $\phi = 0.4$.

In all examples we use the Taylor–Hood $\mathcal{P}_2 - \mathcal{P}_1$ elements for the fluid velocity and pressure in the fracture region, the Raviart-Thomas $\mathcal{RT}_1 - \mathcal{P}_1^{dc}$ elements for the Darcy velocity and pressure, continuous Lagrangian $\mathcal{P}_1$ elements for the displacement, and the $\mathcal{P}_1^{dc}$ elements for the Lagrange multiplier. We use discontinuous piecewise linears $\mathcal{P}_1^{dc}$ for the concentration.

Figure 3 shows the computed velocity and pressure in the reservoir, the displacement, and the velocity in the fracture at the final time $T = 100$s. We observe channel-like flow in the fracture region, from the center to the tips. The leak-off into the reservoir is highest at the fracture tips, but there is also a noticeable leak-off along the fracture length. The structure displacement is small, but it is highest in the vicinity of the fracture and indicates a slight opening of the fracture, as expected.

Figure 4 shows the solution obtained for the concentration at various time moments. At early times, the tracer propagates in accordance with the Stokes velocity field, moving preferentially in horizontal directions towards the tips of the fracture. At later times, despite the small permeability, the tracer penetrates into the reservoir and it is further transported/diffused in it, following the Darcy velocity. We note that, due to the singular shape of the fracture tips, the Darcy velocity at the tips is slightly higher than the Stokes velocity inside the fracture near the tips. This acceleration effect leads to slightly lower concentration values at the fracture tips. This example demonstrates the ability of the method to handle irregularly shaped domains and fractures with a computationally challenging set of parameters.

5.2.2 Example 2: flow and transport through a fractured heterogeneous reservoir

As in the previous example, this example is motivated by hydraulic fracturing, while we illustrate the ability of the method to handle heterogeneous permeability, porosity, and Young's modulus. The domain Ω is given by the rectangle $[0, 1]m \times [-1, 1]m$. A fracture, which represents the fluid domain Ω_f is then positioned in the middle of

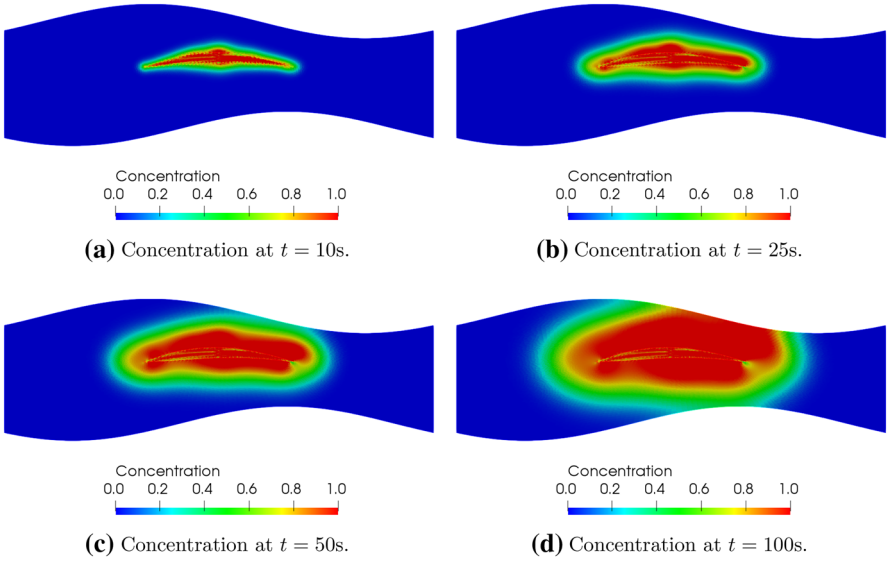

(a) Concentration at $t = 10$s. **(b)** Concentration at $t = 25$s.

(c) Concentration at $t = 50$s. **(d)** Concentration at $t = 100$s.

Fig. 4 Example 1, computed concentration solution

the rectangle, with the boundaries defined by

$$x^2 = 200(0.05 - y)(0.05 + y), \quad y \in [-0.05, 0.05],$$

see Fig. 2b. Fluid is injected into the opening of the fracture on the left boundary. The external boundary of Ω_p is split into $\Gamma_{p,\star}$, where $\star \in \{left, right, top, bottom\}$. The boundary conditions are

$$\begin{aligned}
&\mathbf{u}_f \cdot \mathbf{n}_f = 10, \quad \mathbf{u}_f \cdot \boldsymbol{\tau}_f = 0 && \text{on } \Gamma_{f,inflow},\\
&\mathbf{u}_p \cdot \mathbf{n}_p = 0 && \text{on } \Gamma_{p,left},\\
&p_p = 1000 && \text{on } \Gamma_{p,top} \cup \Gamma_{p,right} \cup \Gamma_{p,bottom},\\
&\boldsymbol{\eta}_p \cdot \mathbf{n}_p = 0 && \text{on } \Gamma_{p,top} \cup \Gamma_{p,right} \cup \Gamma_{p,bottom},\\
&(\boldsymbol{\sigma}_p \mathbf{n}_p) \cdot \boldsymbol{\tau}_p = 0 && \text{on } \Gamma_{p,top} \cup \Gamma_{p,right} \cup \Gamma_{p,bottom},\\
&\boldsymbol{\sigma}_p \mathbf{n}_p = 0 && \text{on } \Gamma_{p,left},\\
&(c\mathbf{u} - \mathbf{D}\nabla c) \cdot \mathbf{n} = (c_{in}\mathbf{u}) \cdot \mathbf{n}, \quad c_{in} = 1 && \text{on } \Gamma_{f,inflow},\\
&(\mathbf{D}\nabla c) \cdot \mathbf{n} = 0 && \text{on } \partial\Omega \backslash \Gamma_{f,inflow}.
\end{aligned}$$

The initial conditions are $\boldsymbol{\eta}_p(0) = 0$ and $p_p(0) = 1000$. The same physical parameters as in Example 1 from Table 2 are used, except for the porosity ϕ, the permeability K, and the Young's modulus E. The permeability and porosity data is taken from a two-dimensional cross-section of the data provided by the Society of Petroleum Engineers (SPE) Comparative Solution Project 10.[1] The SPE data, which is given on

[1] http://www.spe.org/csp.

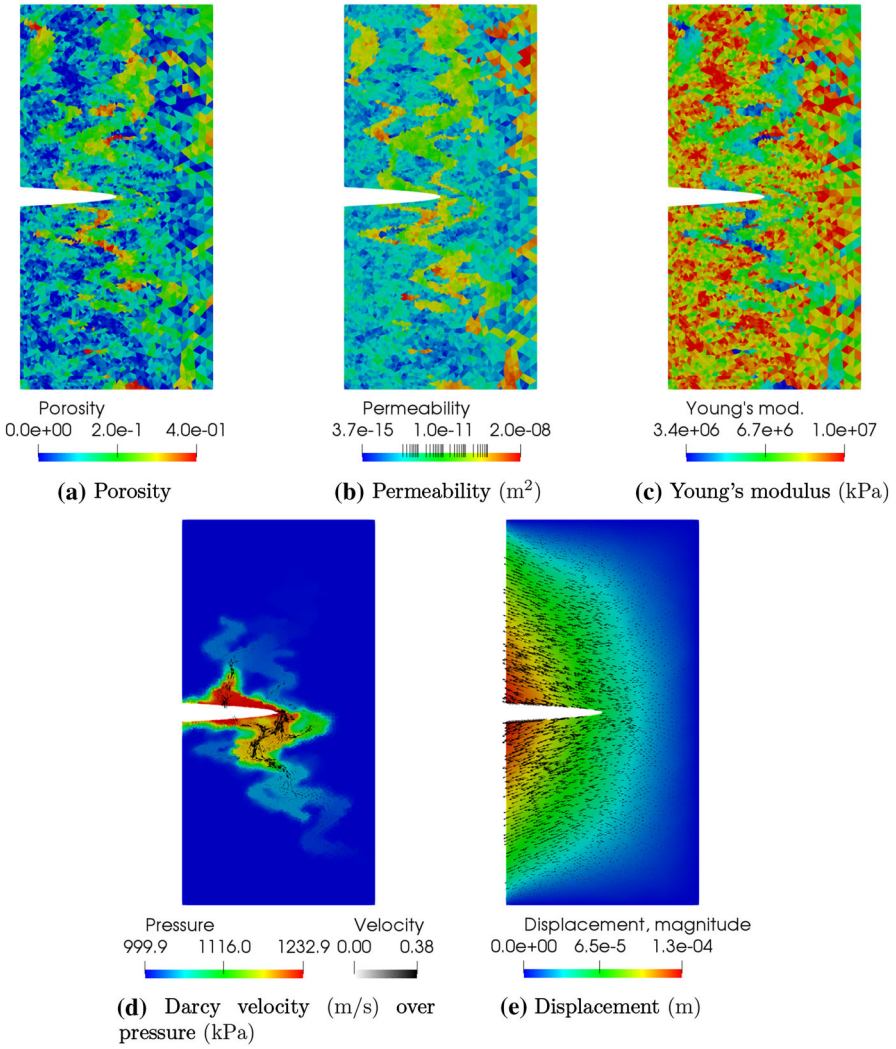

(a) Porosity **(b)** Permeability (m^2) **(c)** Young's modulus (kPa)

(d) Darcy velocity $(\mathrm{m/s})$ over pressure (kPa) **(e)** Displacement (m)

Fig. 5 Example 2, material properties and computed Stokes–Biot solution at $t = 100\,\mathrm{s}$

a rectangular 60×220 grid is projected onto the triangular grid on the domain Ω, and visualized in Fig. 5a–c. We note that the permeability tensor is isotropic in this example. Given porosity ϕ, the Young's modulus is determined from the relationship (Kovacik 1999)

$$E = E_0 \left(1 - \frac{\phi}{\beta}\right)^{2.1},$$

where $E_0 = 10^7$ is the Young's modulus for the non-porous material and the constant $\beta = 0.5$ represents the porosity at which the effective Young's modulus becomes zero.

The computed Darcy velocity, pressure, and displacement at the final time are shown in Fig. 5d, e, respectively. We observe that most of the leak-off is through the fracture tip and the Darcy velocity is largest in a channel-like high permeability region near the tip of the fracture. The displacement field indicates that the fracture opens up as fluid is injected. We also note that the heterogeneities featuring higher permeability and porosity, and correspondingly less stiff material, result in overall larger displacement compared to the previous homogeneous example. Five snapshots of the concentration solution at various time steps are given in Fig. 6. At the early times the tracer propagates along the fracture following the Stokes velocity and penetrates into the high permeability reservoir regions near the middle top, middle bottom, and tip of the fracture. At later times, the tracer is diffused in the poroelastic region; however the overall profile of the concentration front roughly resembles the underlying permeability field.

5.2.3 Example 3: irregularly shaped fluid-filled cavity

The next two examples feature highly irregularly shaped fractures and grids that conform to the fracture geometries. They are motivated by modeling flow and transport through vuggy or naturally fractured reservoirs or aquifers. The domain in this example has a large fluid-filled cavity, see Fig. 2c. The flow is driven from left to right via a pressure drop of 1 kPa. We take the Darcy pressure boundary condition values to be 1 and 0, which can be considered as an offset from a reference pressure. We note that including the reference pressure in the boundary conditions for Darcy and Stokes, the latter being set through $(\boldsymbol{\sigma}_f \mathbf{n}_f) \cdot \mathbf{n}_f$, produces similar results. The boundary conditions are

$$
\begin{aligned}
& p_p = 1 && \text{on } \Gamma_{p,left}, \\
& p_p = 0 && \text{on } \Gamma_{p,right}, \\
& \mathbf{u}_p \cdot \mathbf{n}_p = 0 && \text{on } \Gamma_{p,top} \cup \Gamma_{p,bottom}, \\
& \boldsymbol{\sigma}_p \mathbf{n}_p = 0 && \text{on } \Gamma_{p,left}, \\
& \boldsymbol{\eta}_p = 0 && \text{on } \Gamma_{p,right}, \\
& (\boldsymbol{\sigma}_p \mathbf{n}_p) \cdot \mathbf{n}_p = 0, \quad \boldsymbol{\eta}_p \cdot \boldsymbol{\tau}_p = 0 && \text{on } \Gamma_{p,top} \cup \Gamma_{p,bottom}, \\
& (\boldsymbol{\sigma}_f \mathbf{n}_f) \cdot \mathbf{n}_f = 0, \quad \mathbf{u}_f \cdot \boldsymbol{\tau}_f = 0 && \text{on } \Gamma_{f,right}, \\
& (c\mathbf{u} - \mathbf{D}\nabla c) \cdot \mathbf{n} = (c_{in}\mathbf{u}) \cdot \mathbf{n}, \quad c_{in} = 1 && \text{on } \Gamma_{p,left}, \\
& (\mathbf{D}\nabla c) \cdot \mathbf{n} = 0 && \text{on } \partial\Omega \backslash \Gamma_{p,left}.
\end{aligned}
$$

The physical parameters for this test case are chosen as in the previous example, except for the permeability, which is $K = 10^{-8}\mathbf{I}$ m^2. The total simulation time is 10s, with time step size $\Delta t = 0.1$s.

The velocity fields in the poroelastic and fracture regions are shown in Fig. 7a, c, respectively, while the rock displacement is given in Fig. 7b. The Darcy velocity is largest in the region between the left inflow boundary and the cavity. This results in a larger displacement in this region. The Stokes velocity in the cavity is an order of magnitude larger than in the poroelastic region. A channel-like flow profile is clearly

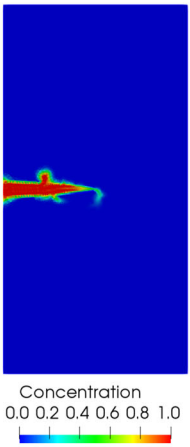

(a) Concentration at $t = 0.5$s.

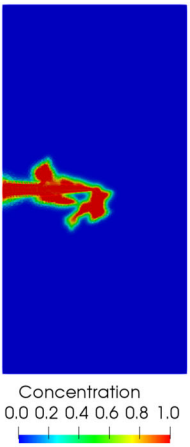

(b) Concentration at $t = 1$s.

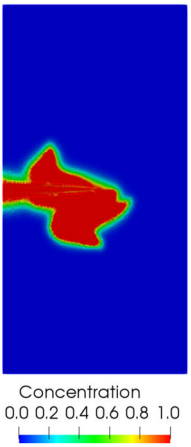

(c) Concentration at $t = 2.5$s.

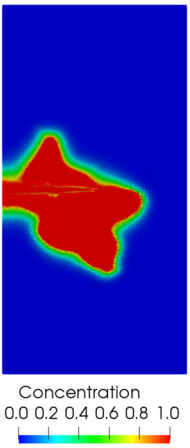

(d) Concentration at $t = 5$s.

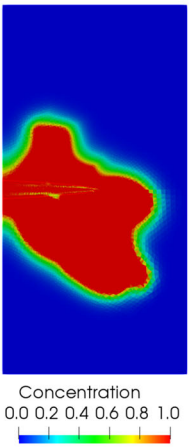

(e) Concentration at $t = 10$s.

Fig. 6 Example 2, computed concentration solution

visible within the cavity, with the largest velocity along a central path away from the cavity walls. Four snapshots of the concentration solution at different time moments are shown in Fig. 8. As expected, the tracer follows the flow, and tends to get into the free fluid region through the nearest fracture tip. After that, it is transported quickly toward the opening in the right boundary, following the Stokes velocity profile and with very little diffusion. In particular, the tracer follows a narrow central path within the cavity away from the walls. This behavior agrees qualitatively with the parameters in the transport equation.

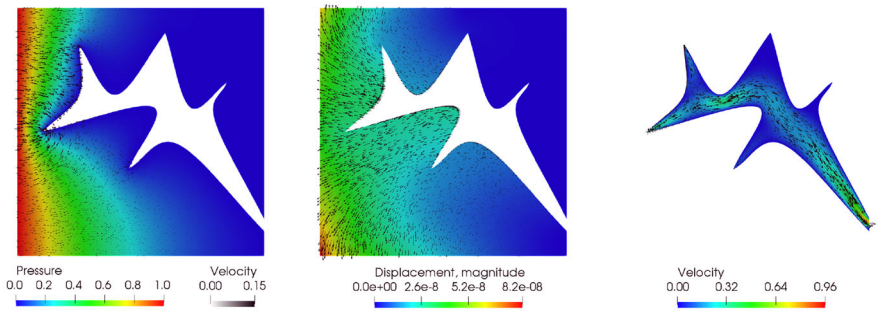

(a) Darcy velocity (m/s) over pressure (kPa) **(b)** Displacement (m) **(c)** Stokes velocity (m/s)

Fig. 7 Example 3, computed velocity, pressure, and displacement fields

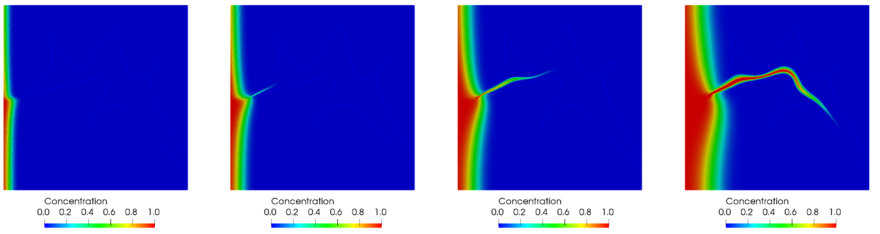

(a) Concentration at $t = 1s$. **(b)** Concentration at $t = 2.5s$. **(c)** Concentration at $t = 5s$. **(d)** Concentration at $t = 10s$.

Fig. 8 Example 3, computed concentration solution

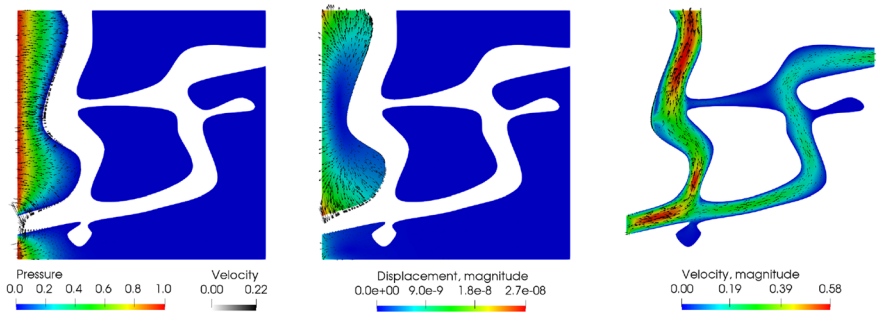

(a) Darcy velocity (m/s) over pressure (kPa) **(b)** Displacement (m) **(c)** Stokes velocity (m/s)

Fig. 9 Example 4, computed velocity, pressure, and displacement fields

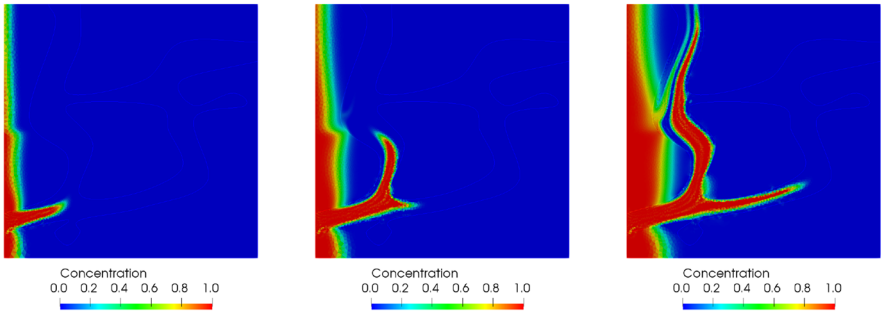

(a) Concentration at $t = 1$s. **(b)** Concentration at $t = 2.5$s. **(c)** Concentration at $t = 5$s.

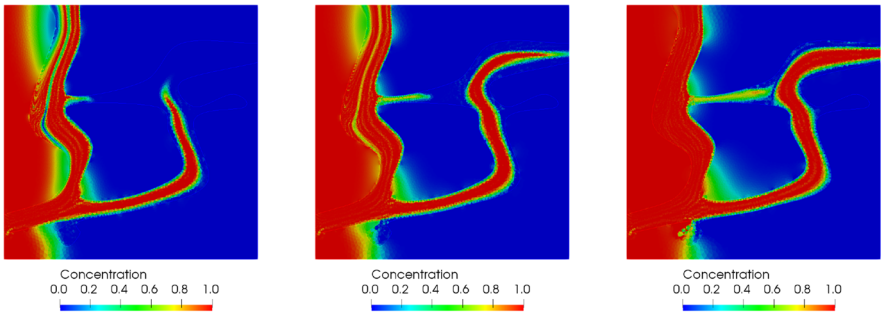

(d) Concentration at $t = 10$s. **(e)** Concentration at $t = 15$s. **(f)** Concentration at $t = 25$s.

Fig. 10 Example 4, computed concentration solution

5.2.4 Example 4: flow through poroelastic media with channel network

The domain for this example is given in Fig. 2d. It features an irregularly shaped network of channels. The physical parameters and boundary and initial conditions for both flow and transport are as in Example 3 except for the boundaries of the Stokes region. Since the channel network has openings at both the left and right boundaries, we set

$$\begin{aligned} &\mathbf{u}_f \cdot \mathbf{n}_f = 0.2, \quad \mathbf{u}_f \cdot \tau_f = 0 && \text{on } \Gamma_{f,left}, \\ &(\boldsymbol{\sigma}_f \mathbf{n}_f) \cdot \mathbf{n}_f = 0, \quad \mathbf{u}_f \cdot \tau_f = 0 && \text{on } \Gamma_{f,right} \cup \Gamma_{f,top}. \end{aligned}$$

We present the computed velocity fields in the poroelastic and fracture regions in Fig. 9a, c and the structure displacement in Fig. 9b. Four snapshots of the concentration solution at different times are shown in Fig. 10. The qualitative behavior of the flow and transport solution is similar to Example 3, with channel-like flow profile and higher velocity within the channel network. The tracer propagates much faster through the channel network, following the widest channel as a preferential path to reach the outflow boundary. Another interesting feature is that in some channels, the tracer enters both from the channel network and from the porous media. Since the diffusion in the channels is very low, this results in two coexisting tracer streams in close proximity to

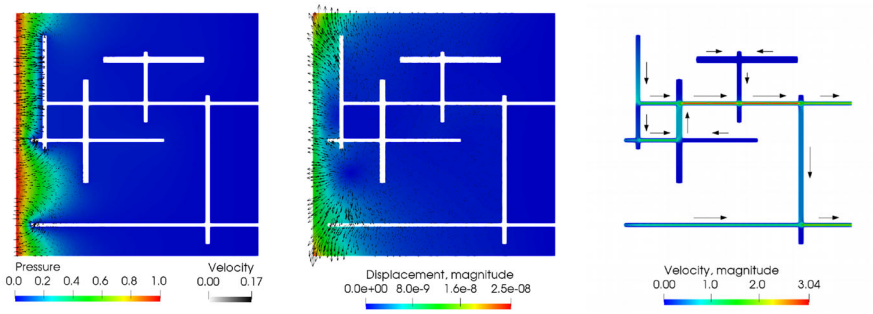

(a) Darcy velocity (m/s) over pressure (kPa) **(b)** Displacement (m) **(c)** Stokes velocity (m/s)

Fig. 11 Example 5, computed velocity, pressure, and displacement fields

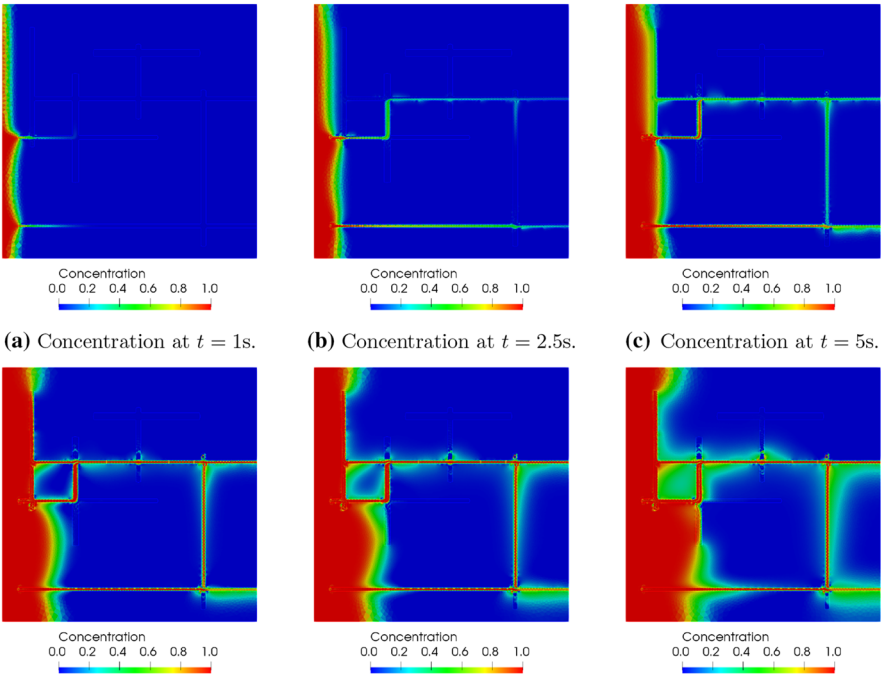

(a) Concentration at $t = 1$s. **(b)** Concentration at $t = 2.5$s. **(c)** Concentration at $t = 5$s.

(d) Concentration at $t = 10$s. **(e)** Concentration at $t = 15$s. **(f)** Concentration at $t = 25$s.

Fig. 12 Example 5, computed concentration solution

each other, but not mixing, being transported by the free fluid, see the upper outflow at time $t = 5$s.

5.2.5 Example 5: flow through poroelastic media with fracture network

The final example is the most challenging, since it involves a network of thin fractures that intersect at sharp angles, see Fig. 2e. The setting for this test case matches the one from Example 4, including physical parameters, initial and boundary conditions, The computed velocity fields in the poroelastic region and the fracture network are visualized in Fig. 11a, c, while the displacement of the porous media skeleton is shown in Fig. 11b. We note that the velocity in the fractures is higher than the velocity in the channels in the previous example, due to the smaller fracture thickness. Also, the velocity is highest in branches of the network where fluid enters from two different branches and that have connection to the outflow boundary. As seen in the plots of the concentration solution in Fig. 12, the tracer is transported quickly through the fractures toward the outflow boundary. Initially it follows well the fracture network geometry, despite the sharp angles between the branches, However, due to relatively small size of the fracture outflow boundaries, the concentration eventually builds up in the fracture region and the tracer starts to penetrate and diffuse into the porous matrix. This can be seen at the later times near the right boundary.

References

Acosta, G., Apel, T., Durán, R., Lombardi, A.: Error estimates for Raviart–Thomas interpolation of any order on anisotropic tetrahedra. Math. Comput. **80**(273), 141–163 (2011)

Aizinger, V., Dawson, C.N., Cockburn, B., Castillo, P.: The local discontinuous Galerkin method for contaminant transport. Adv. Water Resour. **24**, 73–87 (2000)

Ambartsumyan, I., Ervin, V.J., Nguyen, T., Yotov, I.: A nonlinear Stokes–Biot model for the interaction of a non-Newtonian fluid with poroelastic media I: well-posedness of the model. arXiv:1803.00947 (2018a)

Ambartsumyan, I., Khattatov, E., Yotov, I., Zunino, P.: A Lagrange multiplier method for a Stokes–Biot fluid-poroelastic structure interaction model. Numer. Math. **140**(2), 513–553 (2018b)

Arnold, D.N., Brezzi, F., Cockburn, B., Marini, L.D.: Unified analysis of discontinuous Galerkin methods for elliptic problems. SIAM J. Numer. Anal. **39**(5), 1749–1779 (2001/02)

Badia, S., Quaini, A., Quarteroni, A.: Coupling Biot and Navier–Stokes equations for modelling fluid-poroelastic media interaction. J. Comput. Phys. **228**(21), 7986–8014 (2009)

Bazilevs, Y., Takizawa, K., Tezduyar, T.E.: Computational Fluid–Structure Interaction: Methods and Applications. Wiley, New York (2013)

Beavers, G., Joseph, D.: Boundary conditions at a naturally permeable wall. J. Fluid Mech. **30**(1), 197–207 (1967)

Biot, M.: General theory of three-dimensional consolidation. J. Appl. Phys. **12**, 155–164 (1941)

Boffi, D., Brezzi, F., Fortin, M., et al.: Mixed Finite Element Methods and Applications, vol. 44. Springer, Berlin (2013)

Boon, W.M., Nordbotten, J.M., Yotov, I.: Robust discretization of flow in fractured porous media. SIAM J. Numer. Anal. **56**(4), 2203–2233 (2018)

Both, J., Kumar, K., Nordbotten, J.M., Radu, F.A.: Anderson accelerated fixed-stress splitting schemes for consolidation of unsaturated porous media. Comput. Math. Appl. https://doi.org/10.1016/j.camwa.2018.07.033 (2018)

Brenner, S.C.: Poincaré–Friedrichs inequalities for piecewise H^1 functions. SIAM J. Numer. Anal. **41**(1), 306–324 (2003)

Bukac, M., Yotov, I., Zakerzadeh, R., Zunino, P.: Partitioning strategies for the interaction of a fluid with a poroelastic material based on a Nitsche's coupling approach. Comput. Methods Appl. Mech. Eng. **292**, 138–170 (2015)

Bukac, M., Yotov, I., Zunino, P.: An operator splitting approach for the interaction between a fluid and a multilayered poroelastic structure. Numer. Methods Partial Differ. Equ. **31**(4), 1054–1100 (2015)
Bukac, M., Yotov, I., Zunino, P.: Dimensional model reduction for flow through fractures in poroelastic media. ESAIM Math. Model. Numer. Anal. **51**(4), 1429–1471 (2017)
Bungartz, H.-J., Schäfer, M.: Fluid–Structure Interaction: Modelling, Simulation, Optimisation, vol. 53. Springer, Berlin (2006)
Ciarlet, P.: The finite element method for elliptic problems. Class. Appl. Math. **40**, 1–511 (2002)
Cockburn, B., Dawson, C.: Approximation of the velocity by coupling discontinuous Galerkin and mixed finite element methods for flow problems. Comput. Geosci. **6**(3–4), 505–522 (2002). Locally conservative numerical methods for flow in porous media
Cockburn, B., Shu, C.-W.: The local discontinuous Galerkin method for time-dependent convection–diffusion systems. SIAM J. Numer. Anal. **35**(6), 2440–2463 (1998)
D'Angelo, C., Scotti, A.: A mixed finite element method for Darcy flow in fractured porous media with non-matching grids. ESAIM Math. Model. Numer. Anal. **46**(2), 465–489 (2012)
Dawson, C.: Conservative, shock-capturing transport methods with nonconservative velocity approximations. Comput. Geosci. **3**(3–4), 205–227 (1999)
Dawson, C., Sun, S., Wheeler, M.F.: Compatible algorithms for coupled flow and transport. Comput. Methods Appl. Mech. Eng. **193**(23–26), 2565–2580 (2004)
Discacciati, M., Miglio, E., Quarteroni, A.: Mathematical and numerical models for coupling surface and groundwater flows. Appl. Numer. Math. **43**(1–2), 57–74 (2002)
Flemisch, B., Berre, I., Boon, W., Fumagalli, A., Schwenck, N., Scotti, A., Stefansson, I., Tatomir, A.: Benchmarks for single-phase flow in fractured porous media. Adv. Water Res. **111**, 239–258 (2018)
Formaggia, L., Quarteroni, A., Veneziani, A.: Cardiovascular Mathematics: Modeling and Simulation of the Circulatory System, vol. 1. Springer, Berlin (2010)
Frih, N., Roberts, J.E., Saada, A.: Modeling fractures as interfaces: a model for Forchheimer fractures. Comput. Geosci. **12**(1), 91–104 (2008)
Frih, N., Martin, V., Roberts, J.E., Saada, A.: Modeling fractures as interfaces with nonmatching grids. Comput. Geosci. **16**(4), 1043–1060 (2012)
Fumagalli, A., Scotti, A.: A reduced model for flow and transport in fractured porous media with non-matching grids. In: Numerical Mathematics and Advanced Applications 2011, pp. 499–507. Springer, Heidelberg (2013)
Fumagalli, A., Scotti, A.: Numerical modelling of multiphase subsurface flow in the presence of fractures. Commun. Appl. Ind. Math. **3**(1), e–380, 23 (2012)
Galdi, G.P., Rannacher, R. (eds.): Fundamental Trends in Fluid–Structure Interaction. Contemporary Challenges in Mathematical Fluid Dynamics and Its Applications, vol. 1. World Scientific Publishing Co. Pte. Ltd., Hackensack, NJ (2010)
Galvis, J., Sarkis, M.: Non-matching mortar discretization analysis for the coupling Stokes–Darcy equations. Electron. Trans. Numer. Anal. **26**(20), 07 (2007)
Ganis, B., Mear, M.E., Sakhaee-Pour, A., Wheeler, M.F., Wick, T.: Modeling fluid injection in fractures with a reservoir simulator coupled to a boundary element method. Comput. Geosci. **18**(5), 613–624 (2014)
Girault, V., Rivière, B.: DG approximation of coupled Navier–Stokes and Darcy equations by Beaver–Joseph–Saffman interface condition. SIAM J. Numer. Anal. **47**(3), 2052–2089 (2009)
Girault, V., Wheeler, M.F., Ganis, B., Mear, M.E.: A lubrication fracture model in a poro-elastic medium. Math. Models Methods Appl. Sci. **25**(4), 587–645 (2015)
Hecht, F.: New development in FreeFem++. J. Numer. Math. **20**(3–4), 251–265 (2012)
Kim, J., Tchelepi, H.A., Juanes, R.: Stability and convergence of sequential methods for coupled flow and geomechanics: drained and undrained splits. Comput. Methods Appl. Mech. Eng. **200**(23–24), 2094–2116 (2011a)
Kim, J., Tchelepi, H.A., Juanes, R.: Stability and convergence of sequential methods for coupled flow and geomechanics: fixed-stress and fixed-strain splits. Comput. Methods Appl. Mech. Eng. **200**(13–16), 1591–1606 (2011b)
Kovacik, J.: Correlation between Young's modulus and porosity in porous materials. J. Mater. Sci. Lett. **18**(13), 1007–1010 (1999)
Layton, W.J., Schieweck, F., Yotov, I.: Coupling fluid flow with porous media flow. SIAM J. Numer. Anal. **40**(6), 2195–2218 (2003)

Lee, S., Mikelić, A., Wheeler, M.F., Wick, T.: Phase-field modeling of proppant-filled fractures in a poroelastic medium. Comput. Methods Appl. Mech. Eng. **312**, 509–541 (2016a)
Lee, S., Wheeler, M.F., Wick, T.: Pressure and fluid-driven fracture propagation in porous media using an adaptive finite element phase field model. Comput. Methods Appl. Mech. Eng. **305**, 111–132 (2016b)
Lesinigo, M., D'Angelo, C., Quarteroni, A.: A multiscale Darcy–Brinkman model for fluid flow in fractured porous media. Numer. Math. **117**(4), 717–752 (2011)
Martin, V., Jaffre, J., Roberts, J.E.: Modeling fractures and barriers as interfaces for flow in porous media. SIAM J. Sci. Comput. **26**(5), 1667–1691 (2005)
Mikelić, A., Wheeler, M.F.: Convergence of iterative coupling for coupled flow and geomechanics. Comput. Geosci. **17**(3), 455–461 (2013)
Mikelić, A., Wheeler, M.F., Wick, T.: Phase-field modeling of a fluid-driven fracture in a poroelastic medium. Comput. Geosci. **19**(6), 1171–1195 (2015)
Morales, F.A., Showalter, R.E.: The narrow fracture approximation by channeled flow. J. Math. Anal. Appl. **365**(1), 320–331 (2010)
Morales, F.A., Showalter, R.E.: A Darcy–Brinkman model of fractures in porous media. J. Math. Anal. Appl. **452**(2), 1332–1358 (2017)
Oden, J.T., Babuska, I., Baumann, C.E.: A discontinuous *hp* finite element method for diffusion problems. J. Comput. Phys. **146**(2), 491–519 (1998)
Peaceman, D.W.: Fundamentals of Numerical Reservoir Simulation. Elsevier, Amsterdam (1977)
Radu, F.A., Pop, I.S., Attinger, S.: Analysis of an Euler implicit-mixed finite element scheme for reactive solute transport in porous media. Numer. Methods Partial Differ. Equ. **26**(2), 320–344 (2010)
Richter, T.: Fluid–Structure Interactions: Models, Analysis and Finite Elements, vol. 118. Springer, Berlin (2017)
Rivière, B., Yotov, I.: Locally conservative coupling of Stokes and Darcy flows. SIAM J. Numer. Anal. **42**(5), 1959–1977 (2005)
Rivière, B., Wheeler, M.F., Girault, V.: Improved energy estimates for interior penalty, constrained and discontinuous Galerkin methods for elliptic problems. I. Comput. Geosci. **3**(3–4), 337–360 (1999)
Saffman, P.: On the boundary condition at the surface of a porous medium. Stud. Appl. Math. **50**(2), 93–101 (1971)
Scott, R., Zhang, S.: Finite element interpolation of nonsmooth functions satisfying boundary conditions. Math. Comput. **54**(190), 483–493 (1990)
Showalter, R.E.: Poroelastic filtration coupled to Stokes flow. In: Control Theory of Partial Differential Equations, vol. 242. Lecture Notes in Pure and Applied Mathematics, pp. 229–241. Chapman & Hall/CRC, Boca Raton, FL (2005)
Sun, S., Rivière, B., Wheeler, M.F.: A combined mixed finite element and discontinuous Galerkin method for miscible displacement problem in porous media. In: Recent Progress in Computational and Applied PDEs (Zhangjiajie, 2001), pp. 323–351. Kluwer/Plenum, New York (2002)
Sun, S., Wheeler, M.F.: Discontinuous Galerkin methods for coupled flow and reactive transport problems. Appl. Numer. Math. **52**(2–3), 273–298 (2005a)
Sun, S., Wheeler, M.F.: Symmetric and nonsymmetric discontinuous Galerkin methods for reactive transport in porous media. SIAM J. Numer. Anal. **43**(1), 195–219 (2005b)
Vassilev, D., Yotov, I.: Coupling Stokes–Darcy flow with transport. SIAM J. Sci. Comput. **31**(5), 3661–3684 (2009)
Vassilev, D., Wang, C., Yotov, I.: Domain decomposition for coupled Stokes and Darcy flows. Comput. Methods Appl. Mech. Eng. **268**, 264–283 (2014)
Wheeler, M.F., Darlow, B.L.: Interior penalty Galerkin procedures for miscible displacement problems in porous media. In: Computational Methods in Nonlinear Mechanics (Proceedings of Second International Conference, University of Texas, Austin, TX, 1979), pp. 485–506. North-Holland, Amsterdam-New York (1980)